Cell Reports

Article

Microglial Rac1 is essential for experience-dependent brain plasticity and cognitive performance

Graphical abstract

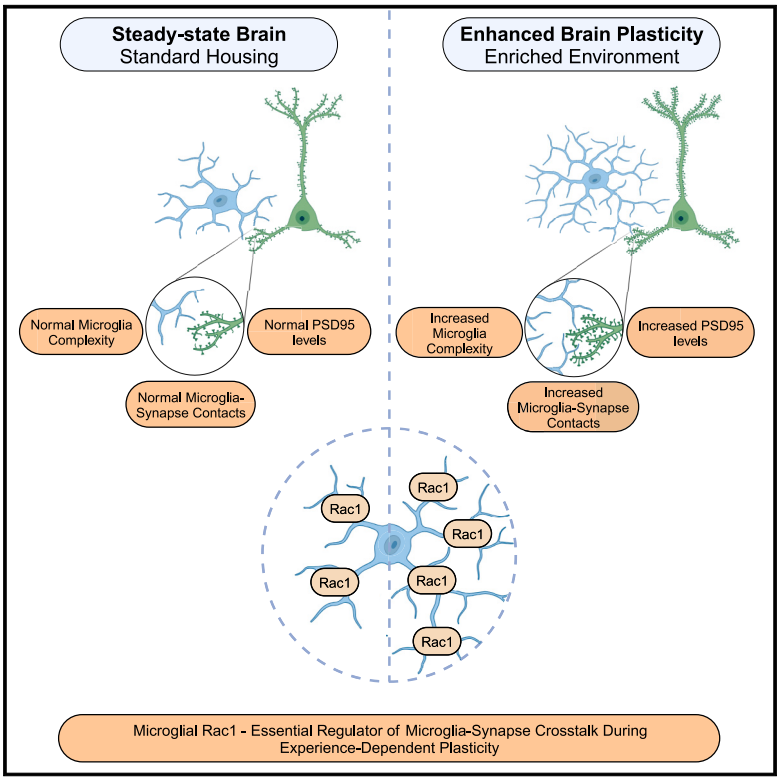

Highlights

- Microglial Rac1 is essential for experience-dependent brain plasticity
- Rac1 modulates microglia-synapse interaction
- Ablation of Rac1 in microglia hampers context-dependent learning, memory, and sociability
- Increasing Rac1 signaling might improve cognitive performance in neurological disorders

Authors

Renato Socodato, Tiago O. Almeida, Camila C. Portugal, ..., Teresa Summavielle, Inês Mendes Pinto, João B. Relvas

Correspondence

renato.socodato@ibmc.up.pt (R.S.), jrelvas@ibmc.up.pt (J.B.R.)

In brief

Socodato et al. show that Rac1 in microglia shapes microglia-synapse interactions, synaptic plasticity, and cognition driven by experience. Loss of Rac1 in microglia disrupts synaptic architecture and impairs experience-dependent learning, memory, and sociability. The work suggests that Rac1 could be a therapeutic target in neurological disorders associated with cognitive deficits.

Socodato et al., 2023, Cell Reports *42*, 113447
December 26, 2023
https://doi.org/10.1016/j.celrep.2023.113447

CellPress

Cell Reports

CellPress
OPEN ACCESS

Article

Microglial Rac1 is essential for experience-dependent brain plasticity and cognitive performance

Renato Socodato,[1,9,*] Tiago O. Almeida,[1,8,9] Camila C. Portugal,[1] Evelyn C.S. Santos,[1,4] Joana Tedim-Moreira,[1,4] João Galvão-Ferreira,[1,4] Teresa Canedo,[1] Filipa I. Baptista,[3] Ana Magalhães,[1] António F. Ambrósio,[3] Cord Brakebusch,[7] Boris Rubinstein,[5] Irina S. Moreira,[6] Teresa Summavielle,[1,2] Inês Mendes Pinto,[1,4] and João B. Relvas[1,4,10,*]

[1]Institute of Research and Innovation in Health (i3S) and Institute for Molecular and Cell Biology (IBMC), University of Porto, Porto, Portugal
[2]ESS.PP, Escola Superior de Saúde do Politécnico do Porto, Porto, Portugal
[3]Center for Innovative Biomedicine and Biotechnology (CIBB), Coimbra Institute for Clinical and Biomedical Research (iCBR), and Clinical Academic Center of Coimbra (CACC), University of Coimbra, Coimbra, Portugal
[4]Department of Biomedicine, Faculty of Medicine of the University of Porto (FMUP), Porto, Portugal
[5]Stowers Institute for Medical Research, Kansas City, MO, USA
[6]Department of Life Sciences, Center for Innovative Biomedicine and Biotechnology (CIBB) and CNC-Center for Neuroscience and Cell Biology, University of Coimbra, Coimbra, Portugal
[7]Molecular Pathology Section, BRIC, Københavns Biocenter, Copenhagen, Denmark
[8]ICBAS - School of Medicine and Biomedical Sciences, Porto, Portugal
[9]These authors contributed equally
[10]Lead contact
*Correspondence: renato.socodato@ibmc.up.pt (R.S.), jrelvas@ibmc.up.pt (J.B.R.)
https://doi.org/10.1016/j.celrep.2023.113447

SUMMARY

Microglia, the largest population of brain immune cells, continuously interact with synapses to maintain brain homeostasis. In this study, we use conditional cell-specific gene targeting in mice with multi-omics approaches and demonstrate that the RhoGTPase Rac1 is an essential requirement for microglia to sense and interpret the brain microenvironment. This is crucial for microglia-synapse crosstalk that drives experience-dependent plasticity, a fundamental brain property impaired in several neuropsychiatric disorders. Phosphoproteomics profiling detects a large modulation of RhoGTPase signaling, predominantly of Rac1, in microglia of mice exposed to an environmental enrichment protocol known to induce experience-dependent brain plasticity and cognitive performance. Ablation of microglial Rac1 affects pathways involved in microglia-synapse communication, disrupts experience-dependent synaptic remodeling, and blocks the gains in learning, memory, and sociability induced by environmental enrichment. Our results reveal microglial Rac1 as a central regulator of pathways involved in the microglia-synapse crosstalk required for experience-dependent synaptic plasticity and cognitive performance.

INTRODUCTION

Microglia, the largest myeloid cell population in the central nervous system (CNS), are best known for their protective roles in the brain.[1] Although long-held as quiescent cells under steady-state conditions, microglia continuously sense and decipher molecular information derived from their local environment.[2,3] Such capability strongly relies on actin cytoskeleton-dependent filopodia-like membrane protrusions and an underlying intracellular signaling machinery built on plasma membrane receptors and second messenger systems.[4] Microglia dramatically change their morphology and adapt their intracellular signaling program in response to environmental signals released by dying neighbor cells or regions undergoing intense synaptic activity.

Targeted gene ablation experiments indicate that microglia-secreted factors are putative modulators of synaptic activity and plasticity.[5–8] Even though the microglial secretome conceivably regulates many aspects of the microglia-synapse crosstalk, little is known about the magnitude and specificity of the alterations in synaptic signaling and remodeling driven specifically by microglia.[9] Remodeling of the synaptic structure and signaling occurs continuously throughout life, and it is crucial for high-order cognitive functions needed for an organism to adapt to different environmental inputs.[10]

Control of actin cytoskeleton reorganization and cell shape, intracellular trafficking involved in the integration of extracellular information, and cell-cell communication by the GTPases of the Rho family, including the most well-characterized members Rac1, RhoA, and Cdc42, make these molecules good candidates to govern microglial sensing capacity and homeostatic mechanisms. In line with this hypothesis, RhoA is a critical negative regulator of microglia immune activation, and its ablation in

adult microglia leads to an Alzheimer's disease-like neurodegenerative process.[7] Although gene-targeting approaches revealed essential modulatory roles for Rac1 in the CNS, including axonal growth and stability,[11] oligodendrocyte myelination,[12] and astrocyte morphology,[13] no information is currently available on Rac1 regulation of microglial functions.

Here, using conditional gene targeting in mice together with a set of complementary approaches, we demonstrate that the loss of Rac1 in adult microglia severely disrupts the microglial ability to sense and interpret their local environment, affecting the microglia-synapse crosstalk required for experience-dependent plasticity and cognitive performance. Furthermore, using multi-omics profiling of microglia, we found that experience-dependent plasticity involves extensive regulation of microglial RhoGTPase signaling (predominantly Rac1), and it is likely to require tight regulation of RhoGTPase-dependent pathways. Our data suggest that modulating RhoGTPase signaling in adult microglia might be useful to devise strategies for boosting neuroplasticity in health and disease.

RESULTS

Conditional ablation of Rac1 in adult microglia

Studies have indicated that Rac1 signaling is affected by aging and brain diseases. In fact, aged mice have shown a significant decrease in Rac1 expression in their brain,[14] which can severely affect microglial function and immune response. Moreover, a correlation has been established between lower Rac1 signaling and Alzheimer's disease,[15,16] which can impact microglial-mediated processes in this context. These findings highlight the critical importance of Rac1 as a molecular target, warranting further investigation in the regulation of microglial functional states.

We aimed to study the effects of targeting Rac1 on adult microglial function, similar to our previous study on RhoA.[7] We crossed Cx3cr1$^{CreER-IRES-EYFP}$ mice[6,17,18] with mice carrying Rac1 floxed alleles[19] to investigate this (Figure 1A). In Cx3cr1^{CreER+} mice, Cre recombinase is induced by tamoxifen administration, and the CreER-IRES-EYFP transgene is active in Iba1^{+} brain cells, including microglia.[6,17,18] We administered tamoxifen to controls and conditional microglia Rac1 mice and analyzed their brains eight weeks later (Figure 1A). Our analysis confirmed a significant reduction of Rac1 mRNA (Figure S1A) and protein levels (Figure 1B) in Cx3cr1^{CreER+}:Rac1$^{fl/fl}$ microglia compared to the controls. Notably, Cx3cr1 haploinsufficiency had no impact on Rac1 mRNA or protein levels in Cx3cr1^{CreER+} microglia (Figures S1A and S1B).

The adverse effects of the CreER-IRES-EYFP transgene in Cx3cr1^{CreER+} mice are mostly limited to the neonatal stage,[20] and we found no differences in the frequency of Rac1^{+} microglia between the genotypes when adult mice did not receive TAM (Figure S1B).

In Cx3cr1^{CreER+} mice, the CreER-IRES-EYFP transgene is active, to a lesser extent, in border-associated macrophages in the brain.[7,21] However, we found no significant alterations in Rac1 mRNA in brain resident macrophages (CD11b^{+}Cd45^{hi} population) or the frequency of brain macrophages in Cx3cr1^{CreER+}:Rac1$^{fl/fl}$ mice (Figure S1C). Similar to brain macrophages and contrasting to microglia, we found no significant changes in Rac1 mRNA or the frequency of macrophage populations in the blood or spleen between the genotypes (Figures S1D and S1E).

We then evaluated the requirement of Rac1 for microglia homeostasis in the adult brain. In agreement with a classical role for Rac1 as a cell shape modifier, we found that adult microglia from Cx3cr1^{CreER+}:Rac1$^{fl/fl}$ mice were hyper-ramified (Figure 1C). The impact of Rac1 on microglial morphology strongly suggests its potential modulation of microglial protrusion dynamics. To investigate this effect, we conducted a comparative analysis of protrusion velocities in HCM3 microglia. Specifically, we overexpressed a dominant-negative form of Rac1 (Rac1-DN) and compared it to wild-type (WT) Rac1. Our results show a significant decrease in protrusion velocity in microglia overexpressing Rac1-DN when compared to cells overexpressing WT Rac1 (Figure 1D). These findings underscore a potential regulatory role of Rac1 in microglial protrusion dynamics and cell motility.

These observed morphological changes in microglia were independent of any Rac1-related effects on microglial cell numbers. Flow cytometry analysis (Figure S1F) and Iba1 immunofluorescence on brain tissue sections (Figure S1G) revealed no difference in microglial cell count between Cx3cr1^{CreER+}:Rac1$^{fl/fl}$ and control groups. Additionally, no significant differences were found in microglial cell death (annexin V^{+} cells), proliferation (Ki67^{+} cells), surface expression of CD11b and CD45, or the number of major histocompatibility complex II^{+} microglia between the two genotypes (Figures S1H–S1L). These findings suggest that Rac1 modulates microglial morphology, but is not necessary for regulating adult microglial numbers or reactivity under steady-state conditions.

Rac1 is dispensable for microglia phagocytosis or ROS production in the steady state

The regulation of active phagocytosis of external ligands (mainly through complement or Fc receptors[22–25]) and the production of reactive oxygen species (ROS) via assembly of nicotinamide adenine dinucleotide phosphate hydrogen oxidases (NOXs)[26,27] are the best-known roles for Rac1 in immune cells. Thus, we evaluated the requirement of Rac1 for phagocytic function and ROS production in steady-state microglia.

To conduct these analyses, we used RNA sequencing (RNA-seq) on microglia isolated through CD11b selection. We chose this method because Rac1 ablation did not affect other myeloid populations during steady state, which reduces any confounding factors in the study of microglial transcriptomics. Furthermore, this approach is widely used in the microglia field and allows for meaningful comparisons with existing transcriptomics datasets.

Following RNA-seq analysis in MACS-separated microglia (flow cytometry confirmed high microglial enrichment by MACS) (Figure 2A), we investigated the requirement of Rac1 for microglia phagocytosis. As such, we performed contingency analysis between the differentially expressed genes (DEGs) regulated by Rac1 in microglia (Figure 2B) (Table S1) and a microglial engulfment module[28] or a module of prospective phagocytic macrophages.[29] Interestingly and unexpectedly, analyses indicated no significant association between the Rac1-regulated DEGs and the microglia engulfment module (odds ratio = 2.12,

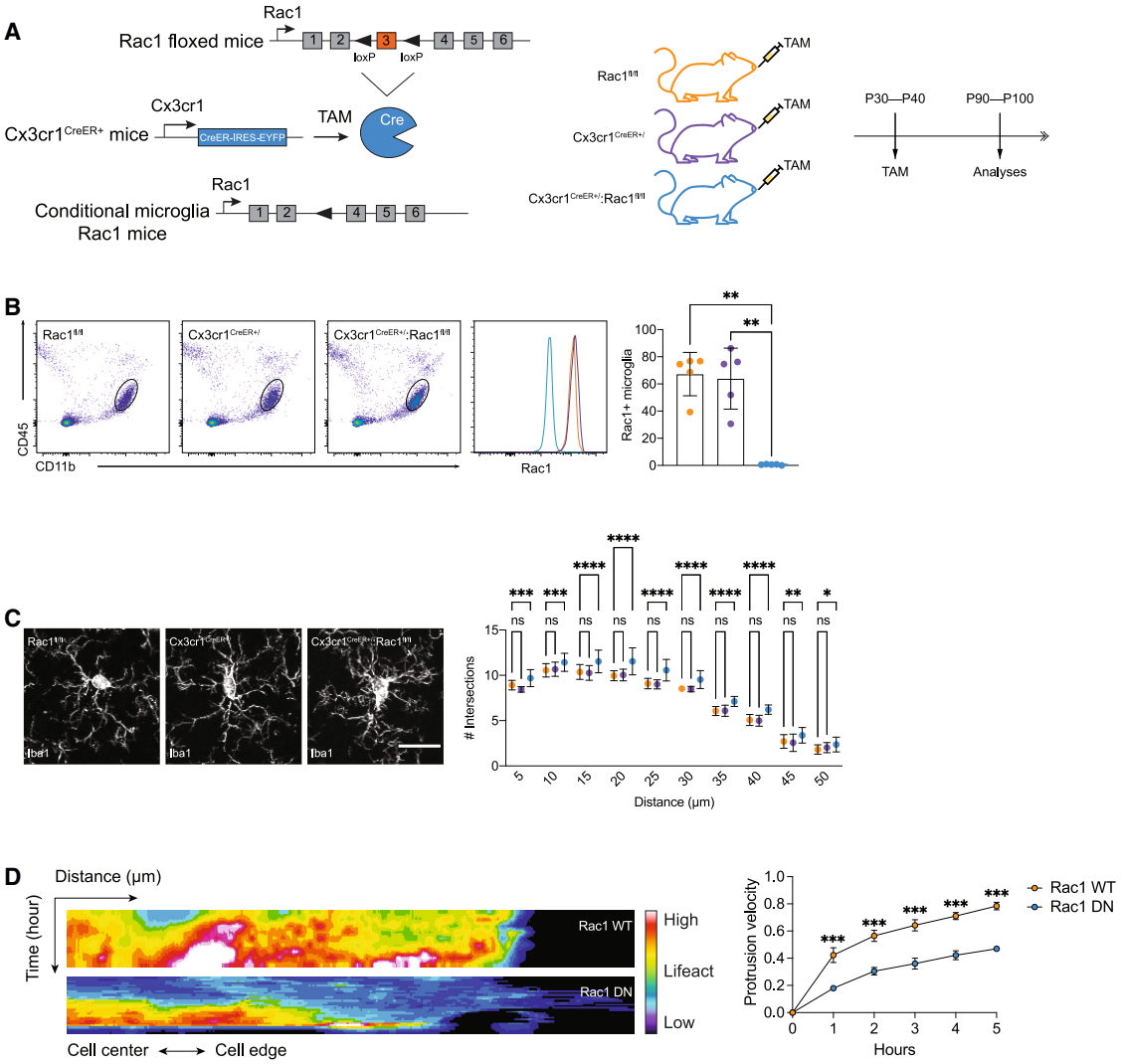

Figure 1. Rac1 ablation in adult microglia

(A) Schematic representation of the strategy used for conditionally ablating Rac1 in adult brain microglia.

(B) Flow cytometry analysis showing Rac1 expression levels in microglia from Rac1$^{fl/fl}$, Cx3cr1^{CreER+}, and Cx3cr1^{CreER+}:Rac1$^{fl/fl}$ mice (n = 5 animals per genotype). The histogram represents the mean with standard deviation (SD) of Rac1+ microglia. **p < 0.01 (one-way ANOVA).

(C) Sholl analysis of Iba1 immunostaining on tissue sections obtained from neocortices of Rac1$^{fl/fl}$, Cx3cr1^{CreER+}, and Cx3cr1^{CreER+}:Rac1$^{fl/fl}$ mice (n = 25 cells from 3 mice per genotype). The histogram displays the mean with SD. *p < 0.05; **p < 0.01; ***p < 0.001; ****p < 0.0001 (two-way ANOVA comparing each distance between genotypes). Scale bar, 10 µm.

(D) Kymograms illustrating the comparison of protrusion velocities between HCM3 microglia overexpressing Rac1-DN and WT Rac1 (Rac1 WT) (n = 9 cells from 3 independent experiments). In both conditions, microglia were transfected with mCherry-Lifeact. Protrusion velocities were measured in µm/min using kymograph analysis. The histogram shows the mean with SD. ***p < 0.001 (two-way ANOVA comparing each time point between WT and DN).

p = 0.38) or the phagocytic macrophage module (odds ratio = 2.31, p > 0.99) (Figure 2C). In line with the RNA-seq data, we confirmed by PCR in flow cytometry sorted microglia from Cx3cr1^{CreER+}:Rac1$^{fl/fl}$, Rac1$^{fl/fl}$, and Cx3cr1^{CreER+} mice the lack of alteration in the amounts of selected mRNA transcripts from the microglia engulfment module (Figure S2A). Then, using double-labeling immunofluorescence on brain tissue sections, we found no significant alterations in the expression of CD68, a glycoprotein mainly associated with the lysosomal compartment and a marker of microglia activity, between Cx3cr1^{CreER+}:Rac1$^{fl/fl}$ and Rac1$^{fl/fl}$ microglia (Figure 2D). To further explore the role of microglia in synaptic engulfment, we examined the phagocytosis of post-synaptic elements, which serves as a direct measure of complement-dependent microglial synaptic engulfment.[30] We found that the amount of post-synaptic material (PSD95^{+}) co-localizing with microglial phagocytic structures (CD68^{+}) was similar in both Cx3cr1^{CreER+}:Rac1$^{fl/fl}$ and Rac1$^{fl/fl}$ littermates (Figure 2E). This finding suggests that the steady-state engulfment activity of adult microglia does not rely on the presence of Rac1. Moreover, this lack of effect on

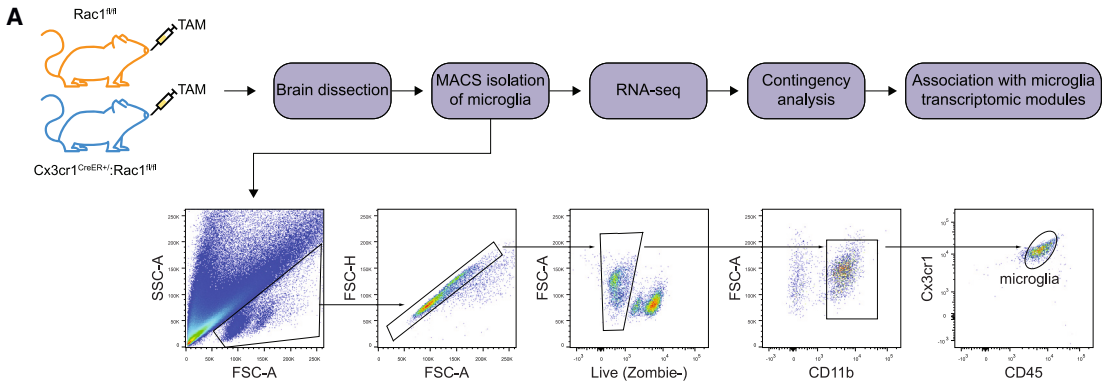

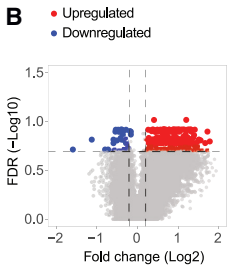

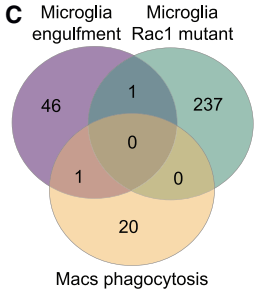

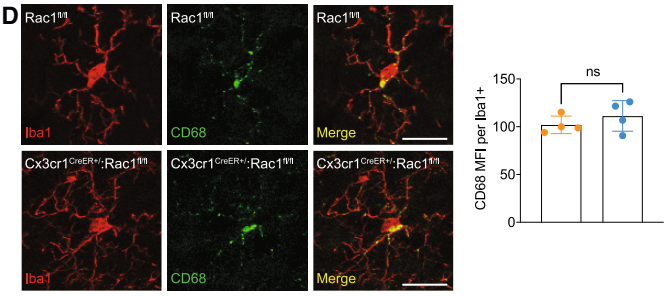

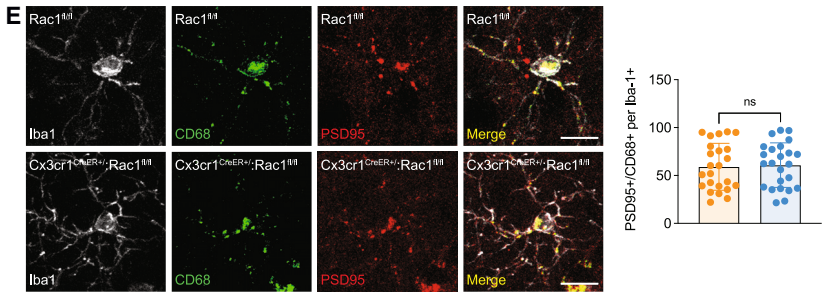

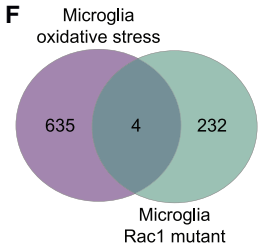

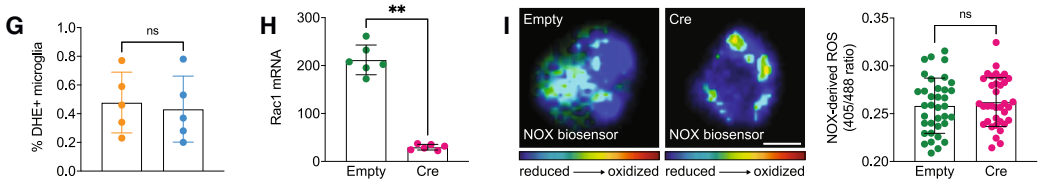

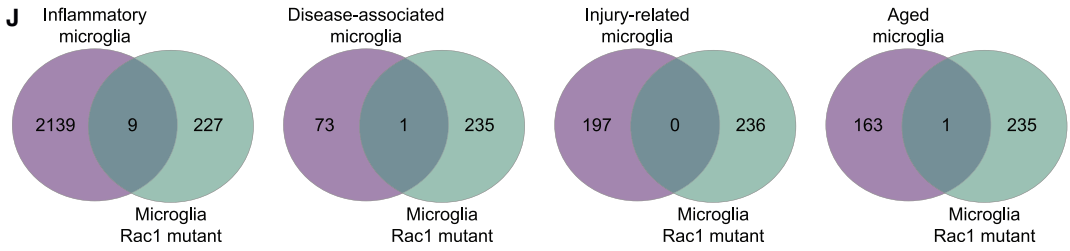

(legend on next page)

engulfment activity did not impact neuronal numbers, as the density of NeuN^{+} cells was comparable between Cx3cr1^{CreER+}:Rac1$^{fl/fl}$ and Rac1$^{fl/fl}$ littermates (Figure S2B).

To investigate the requirement of Rac1 for steady-state microglial ROS generation, we performed a contingency analysis between the microglial RNA-seq-derived DEGs and a transcriptomic module of microglial oxidative stress.[31] These analyses indicated no significant association between the microglia oxidative stress module (odds ratio = 0.62, p = 0.53) and the Rac1-regulated DEGs (Figure 2F). In line with the RNA-seq data, we confirmed by PCR in flow cytometry sorted microglia from Cx3cr1^{CreER+}:Rac1$^{fl/fl}$, Rac1$^{fl/fl}$, and Cx3cr1^{CreER+} mice the lack of alterations in the amounts of selected mRNA transcripts from the microglia oxidative stress module (Figure S2C). Furthermore, we used flow cytometry to study whether the absence of Rac1 in microglia affects their production of ROS. To do this, we injected control and Rac1 mutant mice with the redox-sensitive probe dihydroethidium (DHE) and measured oxidative stress levels in their microglia. The results revealed no significant difference in the frequency of DHE-positive microglia between the genotypes (Figure 2G). This indicates that removing Rac1 from microglia does not have a significant impact on their oxidative stress levels.

Last, using a NOX biosensor,[32] we measured baseline ROS generation derived specifically from NOX in primary microglia lacking Rac1. Primary microglial cultures prepared from Rac1$^{fl/fl}$ brain cortices were first infected with control (empty) lentiviral particles or virus-carrying Cre recombinase (validation of Rac1 ablation is shown in Figure 2H) and then transfected with the NOX biosensor—composed of redox-sensitive GFP fused to the NOX organizer protein p47.[32] As shown in Figure 2I, the amounts of NOX-derived ROS were comparable between control and Cre-infected cultures. We concluded that Rac1 is not a primary redox driver in adult microglia under steady-state conditions.

In addition, contingency analyses (Figure 2J) using known microglial signature modules (including inflammation[33]—odds ratio = 0.69, p = 0.003; disease associated[34]—odds ratio = 1.37, p = 0.52; injury-related[35]—odds ratio = 0.25, p = 0.27; and aging[35]—odds ratio = 0.61, p = 0.99) showed no relevant association with the Rac1-regulated DEGs in steady-state conditions, which was corroborated by PCR (using selected genes of each cluster) in flow cytometry sorted microglia from Cx3cr1^{CreER+}:Rac1$^{fl/fl}$, Rac1$^{fl/fl}$, and Cx3cr1^{CreER+} mice (Figures S2D–S2F).

Rac1 coordinates a signaling program required for microglia-synapse crosstalk

To pinpoint the most relevant biological pathways altered in the microglial transcriptome after Rac1 ablation, we performed preranked gene set enrichment analysis (GSEA) and string ranked enrichment (SRE). GSEA and SRE revealed significant upregulation of 57 and downregulation of 198 biological pathways in microglia, respectively, upon Rac1 ablation (Table S2). Manual trimming and analogy recategorizing relevant pathways to build logical signaling modalities led to the classification of main microglial transcriptomic programs regulated by Rac1: microglial environmental sensing (Table S3) and microglia-synapse crosstalk (Figure 3A).

The microglia-synapse crosstalk program included two modules: intracellular protein trafficking, sorting, and export/secretion, and extracellular matrix (ECM)/growth factor signaling (Figure 3A and Table S4). The protein trafficking/export/secretion module included pathways related to Rab, Ras, and Rho GTPases, Rab-dependent protein trafficking, and cargo flux through microglial endomembranes. The ECM/growth factor signaling module included adhesion/ECM, glial cell line-derived neurotrophic factor/neural cell adhesion molecule (NCAM)-dependent pathway, EPH-ephrin signaling, and synaptic function/transmission (Figure 3A and Table S4).

To understand better the signaling network affected by Rac1 in microglia, we used quantitative label-free phosphoproteomics in MACS-isolated microglia obtained from Cx3cr1^{CreER+}:Rac1$^{fl/fl}$ and control (Rac1$^{fl/fl}$ and Cx3cr1^{CreER+}) mice. After unbiased high-confidence mapping and meticulous phosphosite annotation, we found that the microglial phosphoproteome modulated by Rac1 featured modifications in the abundance of 273 phosphopeptides (corresponding with 206 phosphoproteins), 90 upregulated and 183 downregulated (Figure 3B). To extract consensual information related to microglial signaling

Figure 2. Rac1 is dispensable for microglial engulfment of synaptic elements and ROS production

(A) Workflow of microglial isolation, RNA-seq, and downstream bioinformatics analysis.

(B) Volcano plot showing differentially expressed (DE) transcripts retrieved from RNA-seq. After applying FDR correction, the value of p was less than 0.05.

(C) Venn diagram with contingency analyses between the DE transcripts (RNA-seq) in Cx3cr1^{CreER+}:Rac1$^{fl/fl}$ vs. Rac1$^{fl/fl}$ and transcriptomic programs for microglial engulfment or macrophage phagocytosis.

(D and E) Confocal analysis of Iba1, CD68, and PSD-95 on tissue sections from neocortices of Rac1$^{fl/fl}$ and Cx3cr1^{CreER+}:Rac1$^{fl/fl}$ mice (n = 4 animals per genotype (D) or n = 24 cells from 4 different mice per genotype (E)). Histograms show the mean with SD. Scale bars, 20 μm (D) or 10 μm (E).

(F) Venn diagram with contingency analyses between the DE transcripts (RNA-seq) in Cx3cr1^{CreER+}:Rac1$^{fl/fl}$ vs. Rac1$^{fl/fl}$ and a transcriptomic program of microglial oxidative stress.

(G) Flow cytometry analysis of DHE frequency in microglia from Rac1$^{fl/fl}$ and Cx3cr1^{CreER+}:Rac1$^{fl/fl}$ mice (n = 5 animals per genotype). Histogram shows the mean with SD.

(H) Rac1 mRNA amounts evaluated by qRT-PCR in primary cortical microglia from Rac1$^{fl/fl}$ mice. Cultures were transduced with lentiviruses carrying control or Cre recombinase (n = 6 independent cultures). Histogram displays mean with SD. **p < 0.01 (Mann-Whitney test).

(I) Control or Cre-transduced primary cortical microglia from Rac1$^{fl/fl}$ mice expressing a NOX biosensor were compared. Histogram (mean with SD) shows ratio image changes (n = 36 cells for each condition pooled across 6 different experiments). Pseudocolor ramps display the levels of reduced-to-oxidized ratio values of the biosensor. Scale bar, 10 μm.

(J) Venn diagrams with contingency analyses between the DE transcripts (RNA-seq) in Cx3cr1^{CreER+}:Rac1$^{fl/fl}$ vs. Rac1$^{fl/fl}$ and other microglial transcriptomic programs.

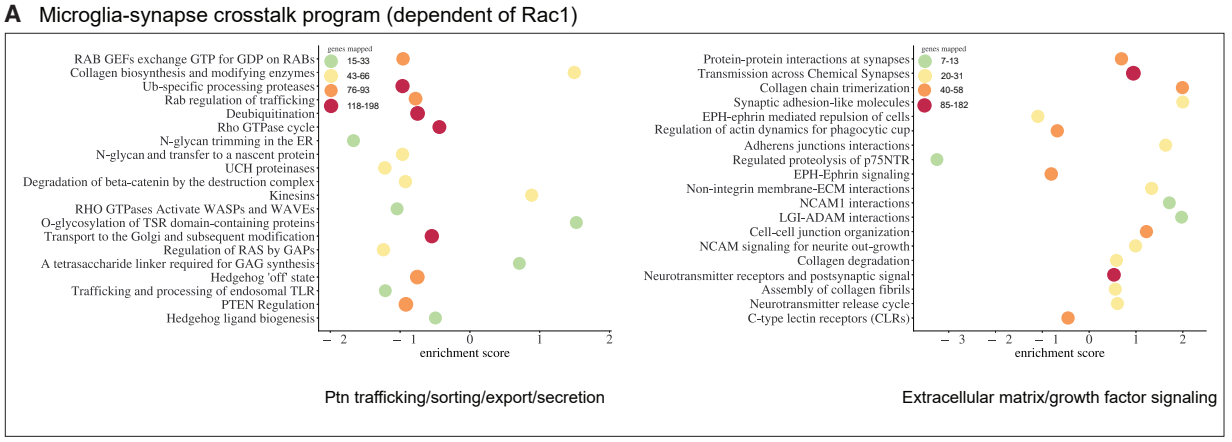

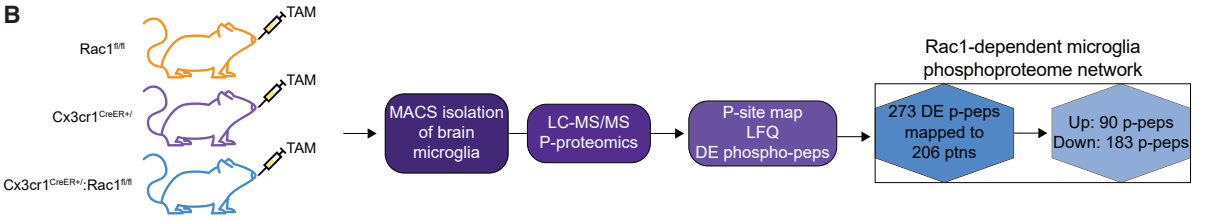

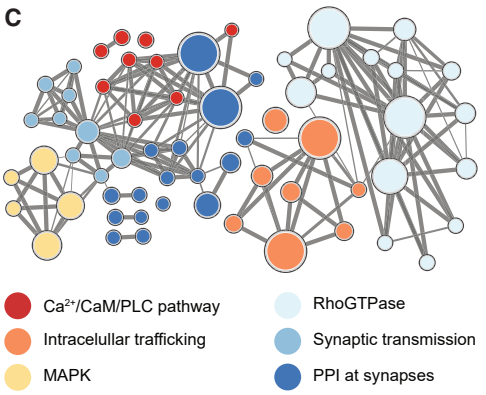

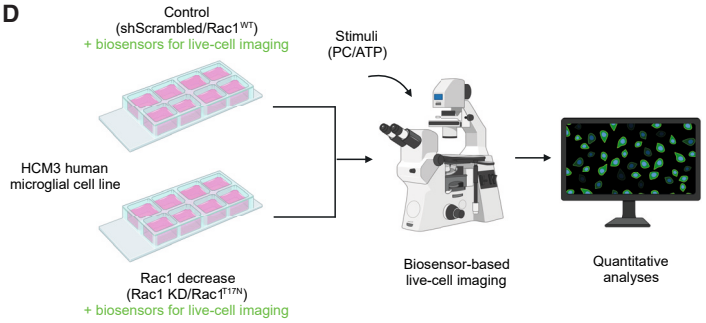

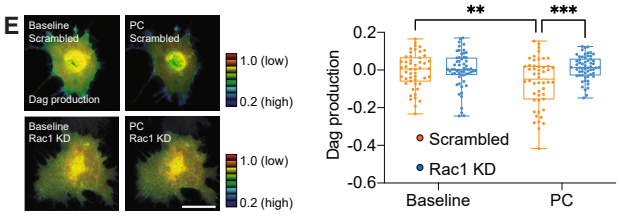

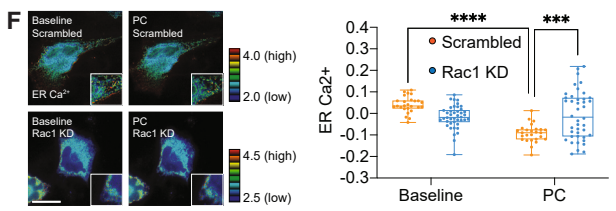

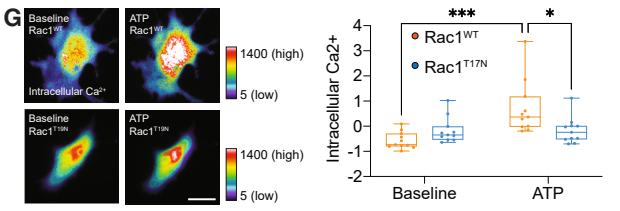

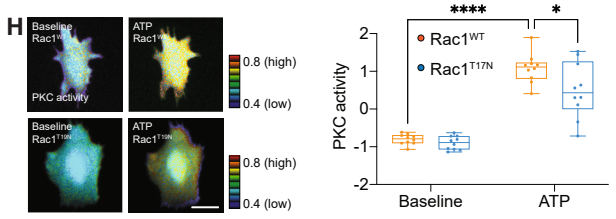

(legend on next page)

transduction, we combined pathway analyses and gene ontology using the 206 matched phosphoproteins and mapped the phosphoproteome-based microglial signaling controlled by Rac1 (Figure 3C and Table S5).

Supporting the Rac1-dependent microglia-synapse crosstalk program (retrieved from RNA-seq data), the Rac1-induced changes in the microglial phosphoproteome were mainly associated with six signaling modules: RhoGTPase and MAPK signaling, intracellular trafficking/vesicular transport, Ca^{2+}/CaM/PLC pathway, protein-protein interaction at synapses, and synaptic transmission (Figure 3C and Table S6).

The RhoGTPase signaling module displayed alterations mainly in Rho activity cycle, Rho-dependent activation of PAKs and ROCKs, and RhoGTPases effectors (including Ppp1r12a, Dync1i1, Prkcb, and non-muscle myosins [Myh9 and Myh10]). The mitogen-activated protein kinase (MAPK) signaling module displayed alterations in BRAF, RAF1, and MAPK1 and MAPK3 pathways. The intracellular trafficking and vesicular transport module displayed alterations in membrane and vesicle trafficking, clathrin-mediated endocytosis, and COPI-mediated anterograde transport. The module of Ca^{2+}/CaM/PLC pathway displayed alterations specifically in calmodulin-induced events, and diacylglycerol (DAG) and IP3 signaling leading to phospholipase C-regulated events. The module of protein-protein interaction at synapses displayed alterations in neurexins and neuroligins, interactions between semaphorins, L1CAM, and L1-ankyrins, and EPH-ephrin signaling. The synaptic transmission module displayed alterations in the release of several neurotransmitter systems along with post-synaptic activity and plasticity, including pathways related to glutamatergic transmission.

To functionally validate the microglial phosphoproteome data, we studied microglial signaling integration via calcium-related pathways using fluorescent biosensors and live-cell imaging in microglial cultures (Figure 3D), as we reported previously.[7,36–38] As key external cues driving calcium-related pathways, we used phosphatidylcholine (PC; a major modulator of microglial lipid cascade) or ATP (a classical danger-associated molecular pattern for microglia). To analyze the lipid sensing cascade, we exposed microglia to PC and measured, in real-time, the local production of Dag (a second messenger generated by phospholipase C activation) and the dynamics of Ca^{2+} between the endoplasmic reticulum (ER) and the cytosol. Using the DagLas biosensor,[39] we observed that PC caused a significant increase in Dag production in the protrusions of control microglia, an effect abrogated in Rac1 knocked down (KD) microglia (Figure 3E). Using the D1ER biosensor,[40] we also found that Rac1 KD significantly blocked the PC-induced release of Ca^{2+} from the ER into the cytosol of microglia (Figure 3F). Then, we studied ATP signaling in Rac1-deficient microglia. We monitored global cytosolic Ca^{2+} mobilization and PKC activity in living microglia to study ATP signaling. Using the Ca^{2+} sensor RGECO[41] and the FRET-based PKC activity reporter CKAR,[42] we observed that ATP increased Ca^{2+} mobilization and PKC activation in microglia overexpressing WT Rac1 (Figures 3G and 3H); however, overexpressing a dominant-negative Rac1 mutant ($Rac1^{T17N}$) attenuated the ATP effect significantly (Figures 3G and 3H).

Overall, our combined RNA-seq, phosphoproteome, and live-cell imaging data raise the hypothesis that microglia modulation of synaptic plasticity through Ca^{2+}-dependent secretion of chemokines, cytokines, and growth factors requires Rac1 signaling.

Experience remodels the microglial signaling network in a Rac1-dependent manner

Experience-dependent plasticity is the capacity of brain cells and circuits to change and adapt to environmental inputs and learning[43] and occurs in brain synapses but also in glial cells. Thus, we ought to demonstrate the magnitude and signaling specificities driven by experience in adult microglia in the presence or absence of Rac1. For that, we used an environmental enrichment (EE) paradigm in which increasing sensory, motor, and cognitive stimulation over standard mouse housing conditions is used to promote experience-dependent brain plasticity. Then, we used quantitative label-free phosphoproteomics in MACS-isolated microglia obtained from $Rac1^{fl/fl}$ and $Cx3cr1^{CreER+}$:$Rac1^{fl/fl}$ mice housed under EE or control environment (CE) (Figure 4A) to pinpoint experience-dependent changes in the microglia.

Figure 3. The microglial Rac1 signature

(A) Rac1-dependent microglia transcriptomic signature revealed by analogy concatenation of GSEA and SRA (n = 3 mice per genotype). Interaction networks display the top enriched pathways.

(B) Workflow of microglial isolation, high-throughput phosphoproteomics, p-site mapping, and downstream bioinformatics analysis for generating Rac1-dependent phosphoproteomic networks. After applying FDR correction, the value of p was less than 0.05 for each phosphosite.

(C) Rac1-dependent phosphoproteomic networks (n = ~4-5 mice per genotype). Networks display the top enriched pathways within each module. Node (pathway) is scaled according to the number of phosphoproteins within it. Edge thickness is scaled according to the degree of pathway crosstalk.

(D) Workflow of biosensor-based live-cell imaging in microglia.

(E) Control (scrambled) or Rac1 KD HMC3 microglia expressing a Dag FRET biosensor were recorded in saline before (t = 0 min; baseline) and after treatment with 10 ng/mL PC. Whisker plots (median and min/max) show time-lapse FRET/donor ratio changes (n = 50–58 cells pooled across 3 different experiments). Pseudocolor ramps display representative ratio values. **p < 0.01; ***p < 0.001 (two-Way ANOVA). Scale bar, 5 μm.

(F) Control (scrambled) or Rac1 KD HMC3 microglia expressing an ER Ca^{2+} FRET biosensor were recorded in saline before (t = 0 min; baseline) and after treatment with 10 ng/mL PC. Whisker plots (median and min/max) show time-lapse FRET/donor ratio changes (n = 26–42 cells pooled across 3 different experiments). Pseudocolor ramps display representative ratio values. ***p < 0.001; ****p < 0.0001 (two-Way ANOVA). Scale bar, 5 μm.

(G) Control ($Rac1^{WT}$) or Rac1 dominant-negative ($Rac1^{T17N}$) HMC3 microglia expressing a cytosolic Ca^{2+} biosensor were recorded in saline before (t = 0 min; baseline) and after treatment with 100 μM ATP. Whisker plots (median and min/max) show time-lapse fluorescence changes (n = 11 cells per group pooled across 3 different experiments). Pseudocolor ramps display representative fluorescence values. *p < 0.05; ***p < 0.001 (two-way ANOVA). Scale bar, 20 μm.

(H) Control ($Rac1^{WT}$) or Rac1 dominant-negative ($Rac1^{T17N}$) HMC3 microglia expressing a PKC FRET biosensor were recorded in saline before (t = 0 min; baseline) and after treatment with 100 μM ATP. Whisker plots (median and min/max) show FRET/donor ratio changes (n = 10 cells per group pooled across 3 different experiments). Pseudocolor ramps display representative ratio values. *p < 0.05; ****p < 0.0001 (two-way ANOVA). Scale bar, 20 μm.

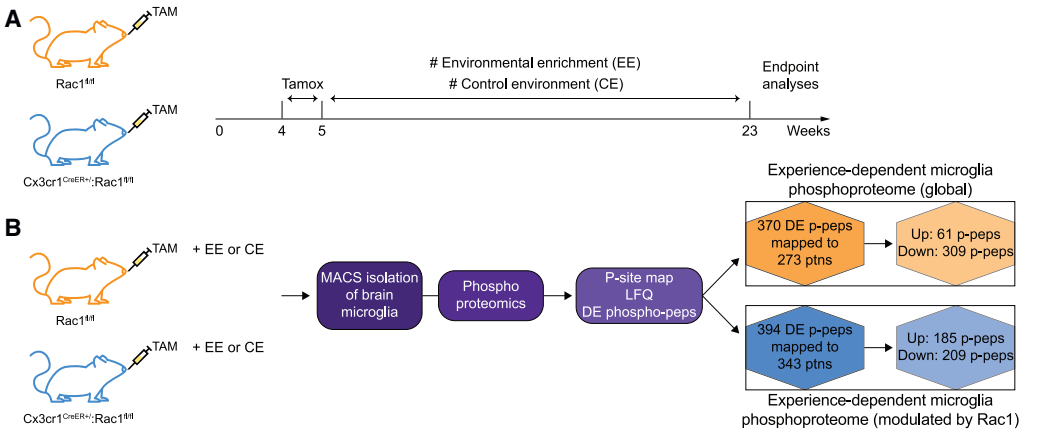

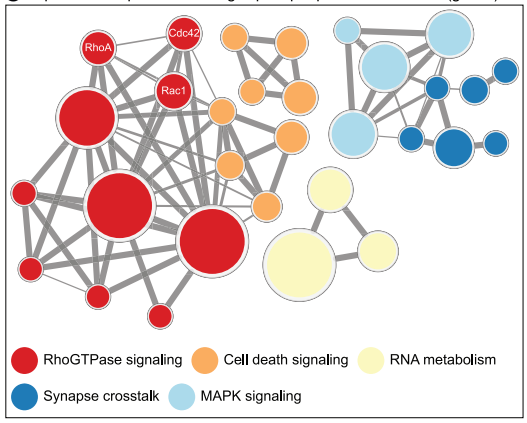

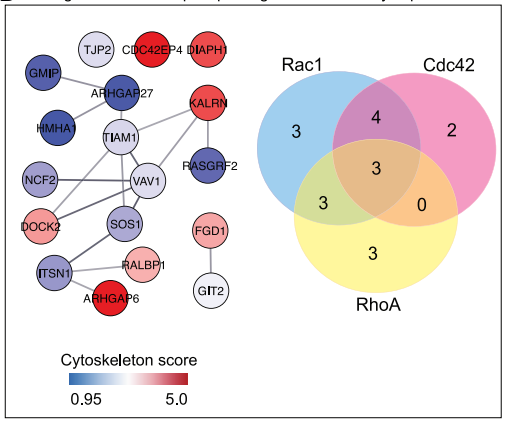

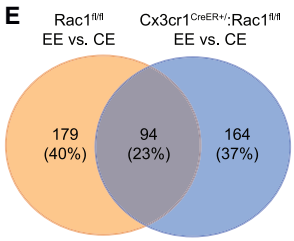

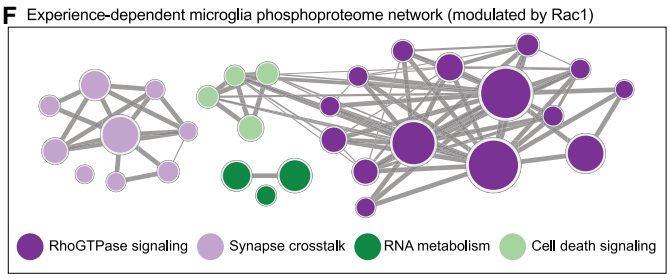

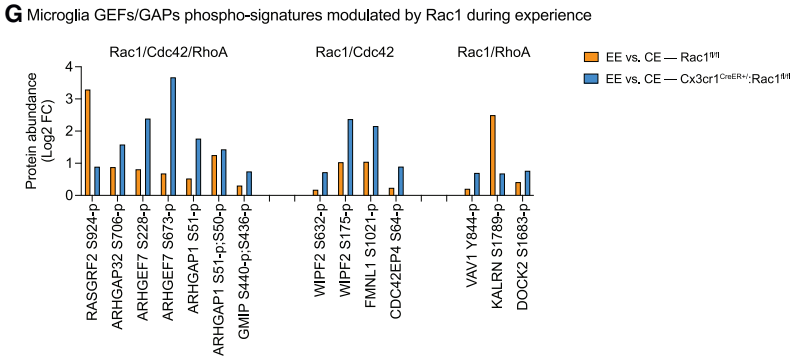

(legend on next page)

To carry out our analyses, we MACS-isolated microglia through P2RY12 selection. This selection method helps to minimize contamination from non-microglial cells, as P2RY12 is exclusively expressed in microglia. The reason for this selection strategy was due to uncertainties regarding the effects of EE on non-microglial myeloid populations. Unlike CD11b, which is expressed by other brain myeloid cells, P2RY12 selection circumvents potential bias in evaluating the impact of EE on microglia in both control and Rac1 mutants.

Analyses of the microglial phosphoproteome driven by experience identified a total of 13,018 raw peptides. Following the removal of low peptide-spectrum matches and non-related post-translational modifications, the number of detected phosphosites was refined to 4,521. Subsequently, applying an FDR cutoff of <0.05 revealed experience-dependent phosphoproteome modifications in control ($Rac1^{fl/fl}$) mice, comprising alterations in 370 phosphopeptides, corresponding with 273 distinct phosphoproteins. Among these modifications, 61 phosphopeptides were upregulated, while 309 phosphopeptides were downregulated (Figure 4B). To extract consensual information related to microglial signaling transduction, we combined pathway analyses and gene ontology using the 273 matched phosphoproteins and found that experience profoundly remodeled the microglial phosphoproteome in control ($Rac1^{fl/fl}$) mice (Figure 4C and Table S7).

Trimming and analogy recategorization of the phosphoproteome dataset allowed the identification of five microglia signaling modules regulated by experience. Specifically, RhoGTPase signaling was the most affected module, followed by synapse crosstalk, MAPK signaling, cell death-related pathways, and RNA metabolism (Figure 4C and Table S7). Importantly, unbiased pathway clustering showed a hierarchical organization of classical RhoGTPase signaling in microglia during experience-dependent plasticity, with Rac1 activity cycle being modulated more prominently by experience than Cdc42 or RhoA activity cycle (Figure 4C and Table S7). Protein-protein interaction (PPI) network integration between Rac1/Cdc42/RhoA modules revealed, as expected, a large redundancy of cytoskeleton-related phospho-guanine nucleotide exchange factor (GEFs) and phospho-GTPase-activating proteins (GAPs) (10/18), with RASGRF2 (S924), ARHGAP45 (S23, S577), and GMIP (S436, S440) being common to the three RhoGTPases modules (Figure 4D). In contrast, SOS1 (S1147), TIAM1 (S358), and NCF2 (T233) were specific to the Rac1 module; FGD1 (T710) and ITSN1 (S971) were specific to the Cdc42 module; and DIAPH1 (S22), ARHGAP6 (S348), and TJP2 (S239) were specific to RhoA module (Figure 4D). These data suggest that RhoGTPase signaling (Rac1 predominantly) might play a pivotal role in the microglia phosphoproteome remodeling during experience-dependent plasticity.

To understand the requirement of Rac1 for experience-dependent phosphoproteome remodeling of microglia, we used integrated analyses with $Cx3cr1^{CreER+}$:$Rac1^{fl/fl}$ mice housed under EE or CE. Then, we combined set theory, gene ontology, and bioinformatics to map the microglia phosphoproteomic modifications related to Rac1 during experience-dependent plasticity. Of 437 phosphoproteins affected by experience in this context, 343 (77%) were modulated by Rac1 (Figure 4E and Table S8). Indeed, the modules associated with microglia RhoGTPase signaling and microglia-synapse crosstalk demonstrated significant dependence on Rac1, whereas the impact of Rac1 on cell death-related pathways and RNA metabolism was relatively minor (Figure 4F). Importantly, Rac1 did not exhibit any effect on the MAPK signaling module in this specific context (Figure 4F).

Furthermore, we observed that EE specifically modulated the phosphorylation levels of various proteins involved in the regulation of Rac1/Cdc42/RhoA signaling modules in control microglia (Figure 4G). However, the ablation of Rac1 hindered the EE-induced changes in the phosphorylation patterns of multiple GAPs and GEFs associated with these signaling modules (Figure 4G). This finding suggests that Rac1 plays a critical role in the hierarchical organization of the microglial RhoGTPase network during experience-dependent plasticity.

Because Rac1 is a key regulator of microglial phosphoproteomic modifications related to experience-dependent plasticity, we investigated whether these molecular changes influenced microglial morphology. To address this, we examined the morphological parameters of microglia in response to EE in both control and Rac1-deficient microglia. First, we quantified the morphological features of microglia, including the number of segments, segment length, segment volume, and the number of segment terminal points, in $Cx3cr1^{CreER+}$:$Rac1^{fl/fl}$ and control $Rac1^{fl/fl}$ mice housed under either EE or CE. In control ($Rac1^{fl/fl}$) microglia under EE conditions, we observed significant changes in all the measured parameters compared to $Rac1^{fl/fl}$ microglia in the CE group. Specifically, the microglia exhibited increased

Figure 4. Experience remodels the microglial phosphoproteome via Rac1

(A) Housing conditions to elicit experience-dependent brain plasticity.

(B) Workflow of phosphoproteomic profiling in microglia after experience-dependent plasticity. After applying FDR correction, the value of p was less than 0.05 for each phosphosite.

(C) Microglial pathways modulated by experience (EE vs. CE) revealed by phosphoproteomic analyses (n = 4 $Rac1^{fl/fl}$ - CE mice and 5 $Rac1^{fl/fl}$ - EE mice). Networks display the top enriched pathways within each module. Node (pathway) is scaled according to the number of phosphoproteins within it. Edge thickness is scaled according to the degree of pathway crosstalk.

(D) Phospho-PPI hubs of Rac1, Cdc42, and RhoA GEFs and GAPs relative to EE vs. CE in $Rac1^{fl/fl}$ mice (retrieved from RhoGTPase signaling module in (C)). Nodes are scaled according to a cytoskeleton score based on the String annotation. The Venn diagram shows the segregation of phospho-GEFs and GAPs across Rac1, Cdc42, and RhoA signaling hubs.

(E) Venn diagram allocating the differentially expressed phosphoproteins across housing conditions and genotypes.

(F) Segregation of microglial pathways modulated concomitantly by experience and Rac1 (n = 4 $Rac1^{fl/fl}$ - CE mice; 5 $Rac1^{fl/fl}$ - EE mice; 4 $Cx3cr1^{CreER+}$:$Rac1^{fl/fl}$ - CE mice; 5 $Cx3cr1^{CreER+}$:$Rac1^{fl/fl}$ - EE mice).

(G) Abundance of selected Rac1, Cdc42, and RhoA phospho-GEFs and GAPs retrieved from the RhoGTPase signaling module in F. Histograms show mean with SD (n = 4–5 mice per group).

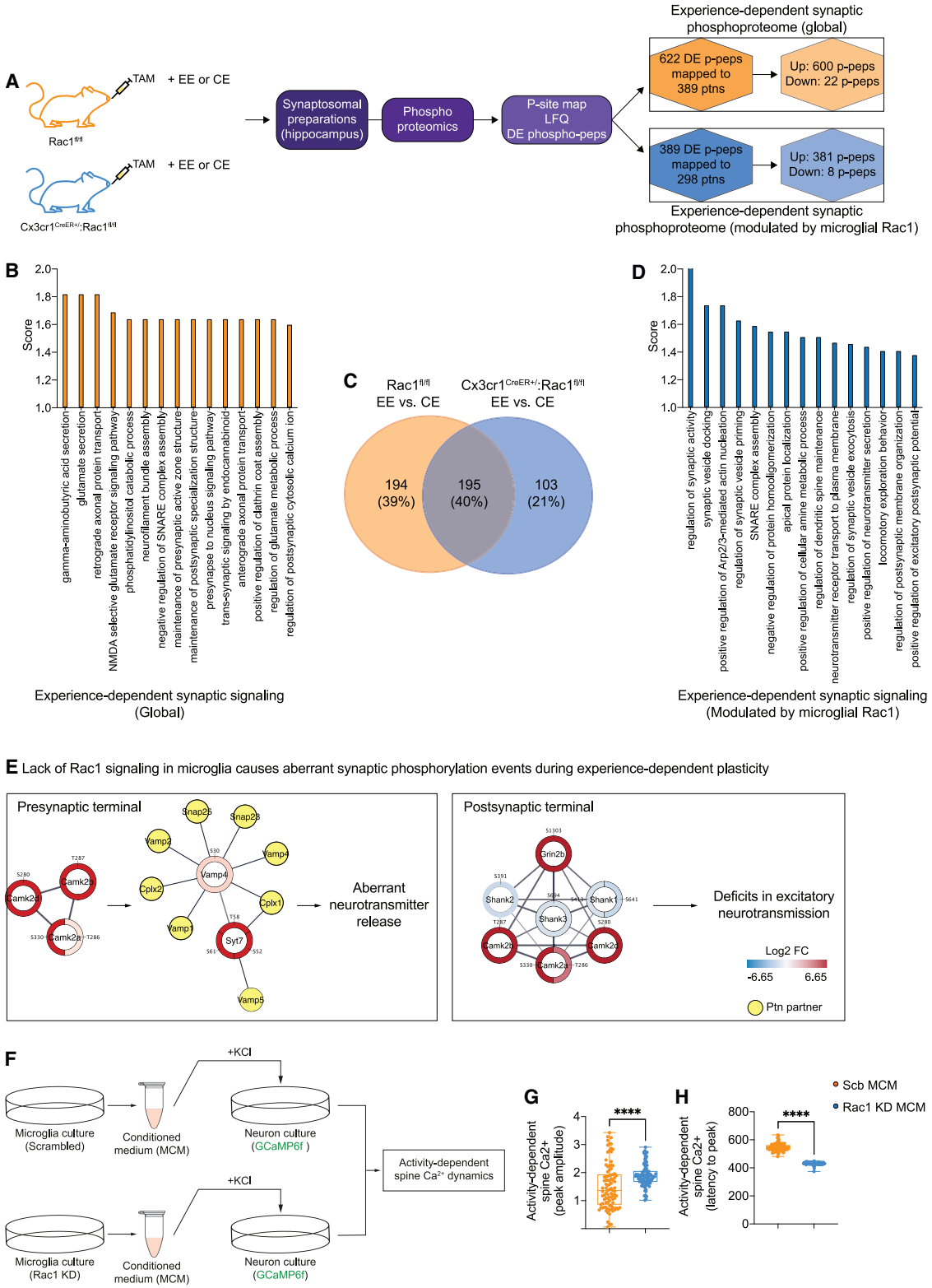

Figure 5. Microglial Rac1 modulates the phosphoproteome plasticity of synapses

(A) Workflow of phosphoproteome profiling in hippocampal synaptosomes after experience-dependent plasticity. After applying FDR correction, the value of p was less than 0.05 for each phosphosite.

(legend continued on next page)

complexity, as reflected by a significantly higher number of segments, larger segment volumes, and an increased number of segment terminal points (Figures S3A and S3B). However, when Rac1 was ablated in Cx3cr1^{CreER+}:Rac1$^{fl/fl}$ mice, we found that the EE-driven changes in microglial morphology were significantly prevented (Figures S3A and S3B). These results demonstrate that Rac1 plays a critical role in shaping the morphological response of microglia during experience-dependent plasticity.

Experience-dependent synaptic phosphoproteome plasticity requires Rac1 signaling in microglia

Could microglial Rac1 signaling affect microglia-synapse cross-talk to impact experience-dependent synaptic remodeling? Experience-dependent synaptic remodeling relies on multi-step phosphorylation of synaptic proteins.[44] Thus, we used quantitative phosphoproteomics in hippocampal synaptosomal preparations obtained from Rac1$^{fl/fl}$ and Cx3cr1^{CreER+}:Rac1$^{fl/fl}$ mice housed under EE or CE (Figure 5A) to elucidate changes in the remodeling of the synaptic signaling modulated by microglial Rac1.

We identified 4,136 raw peptides in the synaptic phosphoproteome influenced by experience. Applying a false discovery rate cutoff of <0.05 and unbiased high-confidence mapping, we observed modifications in the abundance of 622 phosphopeptides (of 3,602), representing 389 phosphoproteins in control mice exposed to EE (Figure 5A). To extract consensual information related explicitly to synaptic pathways, we used over-representation analysis (ORA) with the 389 matched phosphoproteins and found that EE significantly modified over 600 biological processes, 152 molecular functions, and 206 cellular components in the synapses (Figure 5B and Table S9). Pre- and post-synaptic organization, SNARE complex assembly, secretion of neurotransmitters, GABA and glutamate-dependent synaptic signaling, and post-synaptic cytosolic calcium levels were among the top signaling pathways modulated by EE in Rac1$^{fl/fl}$ hippocampus (Figure 5B and Table S9).

Next, employing set theory, we partitioned the pool of synaptic phosphoproteins to isolate those exclusively regulated by microglial Rac1 during EE (Figure 5C and Table S10). By integrating ORA, Gene Ontology, and unbiased PPI clustering, we successfully delineated the synaptic signaling modules that were uniquely associated with microglial Rac1 in response to EE (Figure 5D and Table S10). Specifically, we found that global neurotransmitter release/recycle mechanisms, spine maintenance, post-synaptic architecture, excitatory neurotransmission, and regulation of actin nucleation were the most representative pathways modulated by EE through microglial Rac1 (Figure 5D).

To provide further mechanistic insight into how microglial Rac1-dependent regulation of dynamic phosphorylation events was connected to synaptic function (for instance, neurotransmitter release and excitatory post-synaptic activity) during experience-dependent plasticity, we focused on the prominent Ca^{2+}-dependent synaptic integrator Camk2. After sequence analysis and literature curation, we identified a context- and microglial Rac1-dependent Camk2 circuitry operating simultaneously at pre and post-synaptic compartments (Figure 5E).

Phosphoproteomics profiling detected synaptic supra-phosphorylation of canonical T286 in Camk2a (validated by western blot analyses) (Figure S3C) and T287 in Camk2b, both known to cause kinase overactivation in a microglial Rac1-regulated manner (Figure 5E). Increased phosphorylation of S330, known to control binding to Camk2b, Camk2d, and Camk2g, was also modulated by microglial Rac1 during experience-dependent plasticity (Figure 5E).

At the pre-synapse, microglial Rac1-mediated overactivation of Camk2a most likely disarrayed the fusion machinery for neurotransmitter release (composed of increased phosphorylated forms of Syt7 and Vamp4 and their synaptic partners), leading to an aberrant increase of neurotransmitter release (Figure 5E). At the post-synapse, microglial Rac1-mediated overactivation of Camk2a, elicited by hyperactivity of GluN2B-containing NMDA receptors (hyperphosphorylated at S1303) and derangements of PSD scaffolds (illustrated by decreased phosphorylation of Shank1, 2, and 3), likely compromised the integration of post-synaptic potentials leading to deficits in excitatory neurotransmission (Figure 5E).

These results raise the hypothesis that microglial Rac1 controls neuronal Ca^{2+} dynamics during synaptic activity. To test this hypothesis, we incubated primary cortical neurons with conditioned media obtained from primary microglia expressing control (scrambled MCM) or Rac1 short hairpin RNA (Rac1 KD MCM) and evaluated single-spine Ca^{2+} dynamics during synaptic activity (Figure 5F). Single-spine Ca^{2+} imaging (using the Ca^{2+} sensor GCaMP6f[45]) revealed largely different kinetics of evoked Ca^{2+} responses between scrambled MCM spines (1/slope = 595 au.s^{-1}) and Rac1 KD MCM spines (1/slope = 2099 au.s^{-1}). In agreement with the synaptic phosphoproteome data, such different time-dependent Ca^{2+} kinetics correlated with higher (Figure 5G) and faster (Figure 5H) activity-dependent Ca^{2+} responses in Rac1 KD MCM spines, indicating that loss of Rac1 signaling in microglia leads to aberrant Ca^{2+} dynamics in neuronal spines during synaptic activity.

Overall, these data suggest that Rac1 signaling in microglia is essential for experience-dependent synaptic remodeling.

(B) Synaptic pathways modulated by experience (EE vs. CE) revealed by phosphoproteomic analyses (n = 3 Rac1$^{fl/fl}$ - CE mice; 5 Rac1$^{fl/fl}$ - EE mice). The histogram displays the top enriched pathways.

(C) Venn diagram allocating the differentially expressed phosphoproteins across housing conditions and genotypes.

(D and E) Segregation of synaptic pathways (D) and Camk2-associated phosphoprotein hubs (E) modulated concomitantly by experience and microglial Rac1 (n = 3 Rac1$^{fl/fl}$ - CE mice; 5 Rac1$^{fl/fl}$ - EE mice; 5 Cx3cr1^{CreER+}:Rac1$^{fl/fl}$ - CE mice; 5 Cx3cr1^{CreER+}:Rac1$^{fl/fl}$ - EE mice).). Histograms display the top enriched pathways (D). Hubs with Camk2-associated phosphoproteins are shown (E). Nodes are scaled as log2 fold-change of phosphoprotein abundance.

(F–H) Primary cortical neuronal cultures co-expressing GCamp6f were recorded in saline for 10 min and then recorded for 10 min upon stimulation with conditioned media from primary microglial cultures (MCM) carrying scrambled sequence or Rac1 short hairpin RNA. In all conditions, neurons were co-stimulated with KCl. Whisker plots (median and min/max) show single-spine time-lapse fluorescence changes (n = 90–95 spines pooled across 6 independent neuron cultures). ****p < 0.0001 (Mann-Whitney test).

Rac1 modulates microglia-synapse contacts during experience-dependent plasticity

The interaction between microglia and synapses is crucial in regulating neural circuits. While our data indicate that the microglial secretome may affect the synapse in a Rac1-dependent way, recent evidence shows that microglia-synapse contacts also play a vital role in regulating synapses.[46] To delve into this further, we observed the frequency of microglia-synapse contacts and the resulting synaptic plasticity after exposing control and Rac1 mutant animals to EE.

In control mice, we observed a significant increase in microglia-PSD contacts following EE (as shown in Figure 6A). Moreover, we found that EE promoted structural synaptic plasticity, such as enhanced engulfment of post-synaptic elements (Figure 6B), a higher density of post-synaptic density (PSD) (Figure 6C), and increased synaptic PSD-95 levels (Figure 6D). These findings suggest that EE not only increases microglia-synapse contacts but also promotes structural plasticity through the action of microglia. In contrast, in microglial Rac1 mutants, the expected increase in microglia-synapse contacts following EE was absent (Figure 6A). Furthermore, the anticipated increase in post-synaptic element engulfment, PSD-95 density and expression levels did not occur (Figures 6B–6D). These results support the dependence of microglia-synapse crosstalk and synaptic plasticity on microglial Rac1.

Behavioral testing indicates that microglial Rac1 instructs experience-dependent cognitive performance

Dynamic remodeling of protein phosphorylation networks is critical for cognitive function.[47] So, by remodeling the synaptic phosphoproteome triggered by EE, microglial Rac1 should also impact cognitive performance following EE. In such a way, we conducted different behavioral tests to evaluate the cognitive performance in $Rac1^{fl/fl}$ and $Cx3cr1^{CreER+}$:$Rac1^{fl/fl}$ mice housed under EE or CE (Figure 7A).

First, we assessed contextual memory in the step-down passive avoidance test.[48] Multiple comparisons test revealed an intergroup variation in memory recall (test session latency) (Figure 7B), suggesting that EE and CE might have affected memory retention differently across genotypes. Indeed, comparing the latencies to step-down revealed that EE significantly increased memory retention in $Rac1^{fl/fl}$ mice (Figure 7B), whereas in $Cx3cr1^{CreER+}$:$Rac1^{fl/fl}$ mice the EE-induced improvement in memory retention did not occur (Figure 7B).

Second, we used the novel object recognition (NOR) test to evaluate recognition memory[49] in $Rac1^{fl/fl}$ and $Cx3cr1^{CreER+}$:$Rac1^{fl/fl}$ mice housed under EE or CE. We found that EE increased the discrimination degree of the novel object over the familiar object (Figure 7C) in $Rac1^{fl/fl}$ mice (Figure 7C), indicating that EE improved recognition memory. In contrast, the EE-induced improvement in the NOR performance was blocked entirely in $Cx3cr1^{CreER+}$:$Rac1^{fl/fl}$ mice (Figure 7C).

Third, we used the Y-maze test to evaluate working memory[50] in $Rac1^{fl/fl}$ and $Cx3cr1^{CreER+}$:$Rac1^{fl/fl}$ mice housed under EE or CE. We found that EE significantly decreased the number of arm entry errors, or incorrect arm returns, during the spontaneous maze alternation in $Rac1^{fl/fl}$ mice (Figure 7D), indicating that EE improves spatial working memory. However, the number of wrong arm returns was comparable between EE and CE in $Cx3cr1^{CreER+}$:$Rac1^{fl/fl}$ mice (Figure 7D). Here, we concluded that the EE effect in enhancing spatial working memory requires microglial Rac1.

Last, we used the three-chamber social affiliation test[51] to evaluate social behavior in $Rac1^{fl/fl}$ and $Cx3cr1^{CreER+}$:$Rac1^{fl/fl}$ mice housed under EE or CE. Whereas EE significantly increased $Rac1^{fl/fl}$ mice's preference for exploring the compartment with a stranger animal, EE failed to improve social proximity choices in $Cx3cr1^{CreER+}$:$Rac1^{fl/fl}$ mice (Figure 7E). Here, we concluded that microglial Rac1 signaling modulates experience-dependent social interaction.

Overall, these data suggest that microglial Rac1 instructs experience-dependent learning, memory, and sociability by rewiring the synaptic phosphoproteome.

DISCUSSION

Using inducible microglia-specific gene targeting in mice, RNA-seq, high-throughput phosphoproteomics, and other methodologies, we found that the RhoGTPase Rac1 was required for microglia to sense and interpret their local microenvironment and for microglia-neuron exchanges needed for experience-dependent neuroplasticity.

RhoGTPases work as binary relay switches integrating information from the outside or inside of the cell and disseminating it to various effectors controlling essential cellular functions. The specificity of the information is dictated by the nature of the stimuli, the expression and spatiotemporal activation of GEFs and GAPs, which control RhoGTPase activity (GTP-to-GDP exchange), and effectors downstream of each Rho family member. It is, therefore, no surprise that *in vivo* conditional-gene targeting experiments have revealed that many specific pathways and functions regulated by a given RhoGTPase are cell type, stimulus specific, and context dependent.[52] In line with this, and despite functions classically attributed to Rac1, including the formation of the phagocytic cup,[53] and assembly of the NOX complex,[54] we found no significant association between the Rac1-dependent transcriptomic or phosphoproteomic program and phagocytosis/engulfment or NOX-related ROS signaling in microglia in steady-state conditions. Moreover, no significant changes in the physiological engulfment of post-synaptic elements or ROS production were observed between the brains of control and microglial Rac1 mutants.

Our results also show remarkable specificity for RhoGTPase function in microglia. Comparing the phenotypic outcomes of ablating RhoA[7] or Rac1 in microglia illustrates such specificity. While the lack of RhoA causes spontaneous microglia activation, resulting in neuroinflammation, neuronal loss, and amyloidosis,[7] the absence of Rac1 caused no spontaneous microglia activation, and the synaptic alterations found in microglial Rac1 mutants did not relate to neuroinflammation, oxidative stress, or neuronal loss.

Based on the RNA-seq and phosphoproteome profiling of Rac1-deficient microglia, we hypothesized that microglial activation triggered by extracellular ligands required Rac1 signaling. We combined FRET-based biosensors and live-cell imaging approaches to validate these data functionally. We found that Rac1

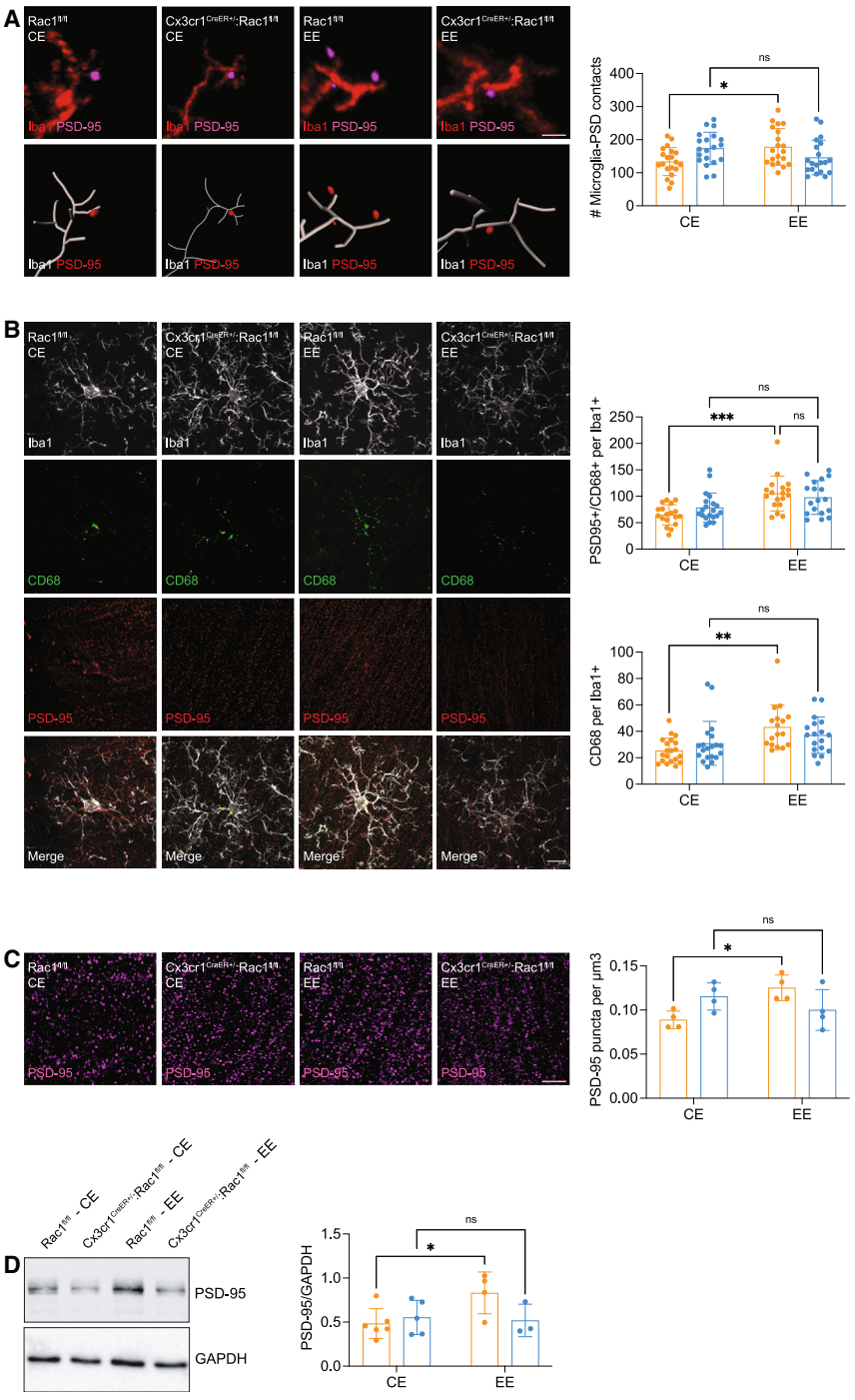

Figure 6. Rac1 modulates microglia-synapse contacts during experience-dependent plasticity

(A) Contacts between microglia and synapses visualized using immunofluorescence and Imaris software. The microglia are labeled with Iba1, and the synapses are labeled with PSD-95. Scale bar, 2 μm.

(B) Confocal image showing the colocalization of Iba1, CD68, and PSD-95, indicating the interaction/engulfment of synaptic elements by microglia. Scale bar, 10 μm.

(C) Confocal image depicting the density of PSD-95. Scale bar, 10 μm.

(D) Western blot for PSD-95 derived from hippocampal synaptosome fractions. GAPDH was the loading control. The graphs represent the mean with SD. *p < 0.05, **p < 0.01, ***p < 0.001 (two-way ANOVA). Genotypes include Rac1$^{fl/fl}$ and Cx3cr1^{CreER+}:Rac1$^{fl/fl}$ mice. Samples sizes in A and B were 18–20 cells pooled across 4 mice per group; in (C), images were averaged from 4 mice per group; for (D), n = 3–6 mice.

controlled many signaling pathways critical for ligand-induced microglial function, including Ca^{2+} mobilization, PKC activity, and lipid sensing.

To investigate Rac1-dependent changes in microglia in a controlled and accessible manner, we used HMC3 cells for live-cell imaging and easier experimental manipulation. Our findings in HMC3 cells demonstrated a strong correlation with *in vivo* data from phosphoproteomics analyses of microglia from Rac1 conditional mice, which suggests that HMC3 cells retain crucial functional properties representative of microglial behavior in the context of our Rac1 study. Collectively, these data suggested that Rac1 signaling regulated pathways necessary for sensing and integrating information from the microglia's local microenvironment.

To further investigate this hypothesis, we used an EE paradigm, exposing mice to increased sensory, motor, and cognitive stimulation beyond standard housing conditions. This approach is known to promote brain plasticity in glial cells and synaptic connections. We then conducted a comprehensive examination of both the microglial signaling network and morphology changes induced by EE, utilizing unbiased phosphoproteomics and confocal-based Imaris 3D rendering. The phosphoproteome analysis revealed that microglial RhoGTPase signaling was the pathway most significantly affected by EE. Within this context, we identified a network of phosphorylated GEFs and GAPs, in which Rac1 emerged as the principal hierarchical regulatory node, followed by Cdc42 and RhoA. Notably, the absence of Rac1 disrupted the architecture of this microglial phospho-GEF/phospho-GAP network. Our findings also demonstrate a critical role for Rac1 in the morphological response of microglia to EE. While some degree of morphological remodeling was still present in Rac1-deficient microglia under EE conditions, it became evident that Rac1 was necessary for the full extent of EE-driven changes in microglial morphology.

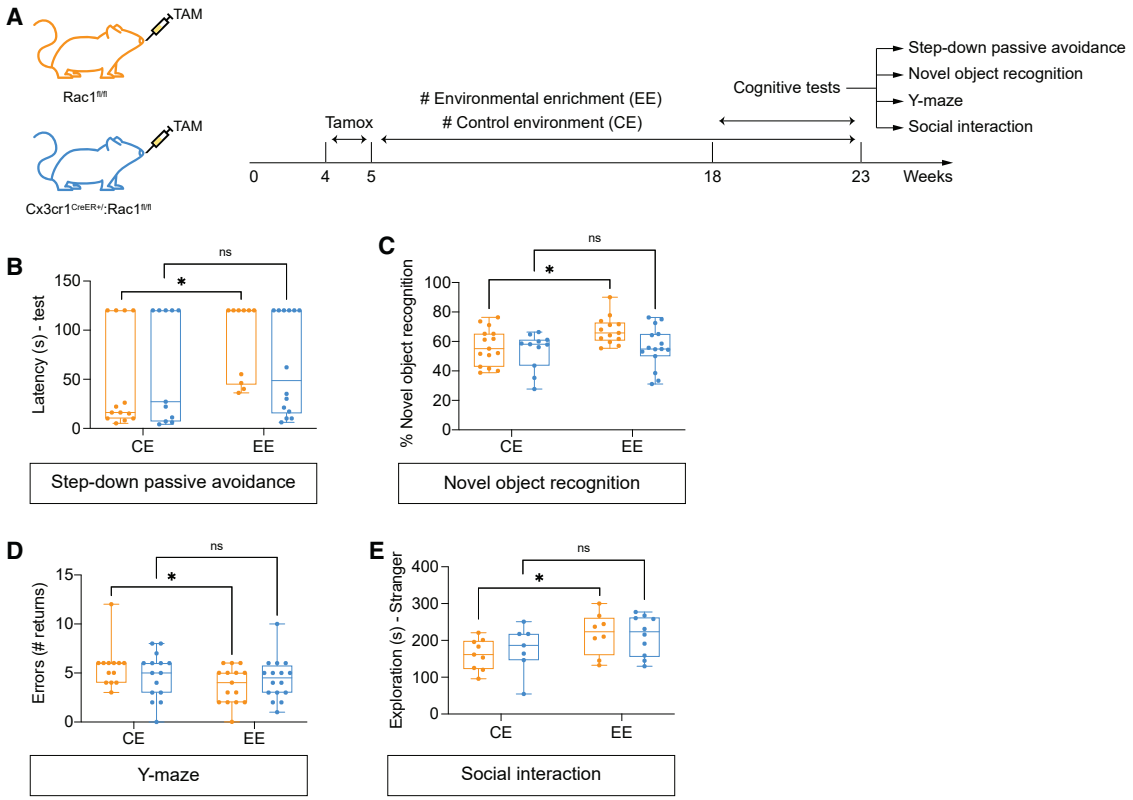

Figure 7. Experience-dependent cognitive performance requires microglial Rac1

(A) Schematics for assessing cognitive performance driven by experience.

(B–E)Evaluation of Rac1$^{fl/fl}$ and Cx3cr1^{CreER+}:Rac1$^{fl/fl}$ mice in the step-down passive avoidance (B), NOR (C), Y-maze (D), and three-chamber social interaction tests (E). Whisker plots show the median, quartiles, and min/max. Each dot represents a mouse. *p < 0.05 (two-way ANOVA).

This strongly suggests that Rac1 plays an important role in the hierarchical organization of the microglial RhoGTPase network, which in turn governs microglial responses to experience-dependent plasticity, encompassing both signaling modifications and morphological adaptations.

Since microglia are critical regulators of synaptic function and plasticity, we investigated synaptic plasticity in the context of EE following the ablation of microglial Rac1. Microglia-synapse crosstalk may occur through direct physical contact between microglia and synaptic elements,[55] microglia-mediated ECM remodeling around synapses[5] or activation of synaptic receptors by microglia-secreted molecules (secretome).[6,7] Remodeling of neuronal circuitries allows the brain to continuously change and adapt to new experiences and relies mainly on multistep modifications of synaptic proteins, including the modulation of their expression[56] and phosphorylation.[44]

We employed a comprehensive, multi-disciplinary strategy that involved RNA sequencing, phosphoproteomics, tissue immunolabeling, and live-cell imaging to deepen our understanding of the potential influence of microglial Rac1 on synaptic plasticity. Our results revealed a significant role of Rac1 signaling in the microglia-triggered release of various substances, including chemokines, cytokines, and growth factors, all of which may have a profound impact on synaptic plasticity. Moreover, our data underscored an increased frequency of physical interactions between microglia and synapses during experience-dependent plasticity. Such contacts could drive multiple synaptic processes, such as pruning, remodeling, and plasticity, all of which are also paramount for synaptic function. Thus, our findings suggest that the microglia-mediated modulation of synaptic plasticity is orchestrated not only by the secretory products released into the synapses but also through direct physical interactions with synaptic elements. This illuminates the importance of microglial Rac1 signaling in shaping synaptic plasticity driven by EE.

Microglia-specific ablation of Rac1 combined with high-throughput phosphoproteomics allowed us to map and specify a microglia-dependent synaptic phosphoproteome signature driven by experience. As such, our phosphoproteome data further support the emergent notion of proteome plasticity, in which the proteome signature of an organism adapts to long-term changes in the external environment.[57]

Our data suggest that the microglia-dependent synaptic phosphoproteome arranged itself in an intricate signaling network that probably crosstalks continuously with the local synaptic transcriptome[58] during activity-dependent plasticity. The substantial overlap of synaptic phosphoproteins (our datasets) and many mRNA species present at synaptic sites (e.g., CamK2a, PKC, PKA, NMDA receptor subunits, and actin cytoskeleton-related)[58] not only illustrates a bidirectional modulation between the synaptic transcriptome and phosphoproteome,[5] but also

supports a role for microglia in modulating experience-dependent plasticity via Rac1 signaling.

ECM remodeling can induce NCAM-dependent spine formation and post-synaptic assembly,[59] whereas loss of NCAM decreases synapse numbers[60] and disrupts learning and memory.[61] A post-synaptic adhesion complex formed by NCAM, βI-spectrin, and NMDA receptors promotes post-synaptic Ca^{2+} dynamics, recruiting and activating CamK2a to modulate synapse formation.[62] Our functional live-cell imaging assays demonstrated aberrant activity-dependent Ca^{2+} dynamics and spine remodeling in neurons exposed to the conditioned media of Rac1-deficient microglia. In line with this, the synaptic phosphoproteome profiling showed alterations in NCAM, spectrins, NMDA receptors, and CamK2a in the synaptosomes of microglial Rac1 mutants during experience-dependent plasticity.

The fact that microglial Rac1 shaped the phosphoproteome signature of the synapses logically suggested that it also impacted cognition. Accordingly, previous studies using conditional gene ablation have reported that microglia are involved in cognitive functions.[5–7,63,64] Our behavioral testing indicated that microglial Rac1 also controlled experience-dependent cognitive enhancement by remodeling the synaptic phosphoproteome. Moreover, based on the microglia's phosphoproteome, we could predict the alterations in the synaptic signaling that we later obtained by directly profiling the phosphoproteome in the synaptosomes.

Synaptic remodeling ultimately governs the encoding and storage of new experiences in the brain, consequently dictating behavioral adaptations to different environmental scenarios. We triggered experience-dependent synaptic remodeling using an EE paradigm. It is well accepted that the molecular and cellular changes that EE produces in the brain correlate with enhanced cognitive function.[65] Indeed, we found that control mice housed under EE displayed notorious improvements in learning, memory, and social plasticity, confirming that EE enhances cognitive performance. However, EE produced no cognitive enhancement in microglial Rac1 mutants. The vast differences in the phosphoproteome signature in the hippocampal synapses of microglial Rac1 mutants somewhat explain why EE failed to function as a cognitive enhancer in these mice. Hence, synaptic phosphoproteome profiling and behavioral testing indicated that microglia were required to trigger synaptic plasticity-related pathways connected to high-order cognitive functions.

Overall, we described essential and specific roles of Rac1 for microglial homeostatic functions, microglia-synapse crosstalk, and adult brain plasticity. Combining microglial Rac1 ablation with synaptosome proteomic profiling allowed us to characterize a microglia-dependent synaptic phosphoproteome signature driven by experience. Furthermore, integrating behavioral analyses in mice lacking Rac1 in adult microglia revealed microglia as a modulator of experience-driven cognitive enhancement. Ultimately, mapping and specifying the synaptic changes mediated by microglia might have broad implications for devising strategies to enhance cognitive performance or compensate for the cognitive decline during aging or brain disease.

Limitations of the study

While our study provides valuable insights, it is important to note its limitations. Since our research primarily used mice as the main model organism, one should exercise caution when attempting to extrapolate the results to human physiological contexts. Additionally, some of our data relied on cultured cells for live-cell imaging, which, while showing a promising correlation with *in vivo* data, may not fully capture the intricacies of endogenous systems. Furthermore, it should be noted that the study's focus on Rac1's role in microglia and synaptic plasticity may obscure the potential significance of other molecules and pathways integral to these processes. The chosen EE paradigm, designed to enhance brain plasticity, may have effects that are uniquely tied to its specific conditions, limiting broader interpretations. Lastly, the behavioral tests conducted on mice may not accurately reflect human cognitive processes, and such tests inherently come with variability, which further complicates the extrapolation of the findings to human behavior.

STAR★METHODS

Detailed methods are provided in the online version of this paper and include the following:

- KEY RESOURCES TABLE
- RESOURCE AVAILABILITY
  - Lead contact
  - Materials availability
  - Data and code availability
- EXPERIMENTAL MODEL AND STUDY PARTICIPANT DETAILS
  - Animals
  - Microglial cell line
  - Primary microglial cultures
  - Primary cultures of cortical neurons
- METHOD DETAILS
  - Environmental enrichment protocol
  - Behavioral tests
  - Tissue preparation and immunofluorescence
  - Confocal imaging and morphometric analysis
  - IMARIS Analysis
  - Flow cytometry and cell sorting
  - MACS isolation of microglia
  - Library preparation, Sequencing, and Bioinformatics
  - Gene expression by qRT-PCR
  - Phospho-proteomics sample preparations
  - High-throughput proteomics data acquisition and quantification
  - Phosphoproteome bioinformatic analyses
  - Western blotting
  - Biosensor-based live-cell imaging
  - Protrusion Velocity Measurements in Cultured Microglia
  - Collection of microglia-conditioned media (MCM)
  - Single-spine calcium imaging
- QUANTIFICATION AND STATISTICAL ANALYSIS

SUPPLEMENTAL INFORMATION

Supplemental information can be found online at https://doi.org/10.1016/j.celrep.2023.113447.

ACKNOWLEDGMENTS

Work in the JBR laboratory was financed by Portuguese funds through FCT—Fundação para a Ciência e a Tecnologia/Ministério da Ciência, Tecnologia e Ensino Superior in the framework of the project PTDC/MED-NEU/1677/2021. Work in the TS laboratory was financed by Portuguese funds through FCT—Fundacao para a Cie^ncia e a Tecnologia/Ministério da Cie^ncia, Tecnologia e Ensino Superior in the framework of the project PTDC/SAU-TOX/0067/2021 and 2022.03699.CEECIND. I.M.P. acknowledges funding from European Union's Seventh Framework Program for research, technological development and demonstration (Marie Curie Actions) under grant agreement no 600375. C.C.P. and R.S. hold employment contracts financed by national funds through FCT—in the context of the program-contract described in paragraphs 4, 5, and 6 of art. 23 of Law no. 57/2016, of August 29, as amended by Law no. 57/2017 of July 2019. T.O.A. and J.T.M. were financed by the FSE - Fundo Social Europeu - through Norte2020 - Programa Operacional Regional Norte and by Portuguese funds through FCT - Fundação para a Ciência e Tecnologia/Ministério da Ciência, Tecnologia e Ensino Superior. FCT scholarship references: SFRH/BD/147981/2019 and UI/BD/151552/2021. The authors acknowledge the support of the following i3S Scientific Platforms: Advanced Light Microscopy (A.L.M.), a member of the national infrastructure PPBI-Portuguese Platform of BioImaging; Animal Facility; Cell culture and Genotyping; Genomics; Proteomics; and Translational Cytometry.

AUTHOR CONTRIBUTIONS

Conceptualization—R.S., C.C.P., A.F.A., C.B., T.S., and J.B.R.; formal analyses—R.S., T.O.A., J.G.F., B.R., I.S.M., and I.M.P.; funding acquisition—R.S., A.F.A., T.S., I.M.P., and J.B.R.; investigation—R.S., T.O.A., C.C.P., E.C.S.S., J.T.M., J.G.F., T.C., F.I.B., and A.M.; resources—A.F.A., C.B., T.S., I.M.P., and J.B.R.; supervision—R.S. and J.B.R.; validation—R.S., T.O.A., C.C.P., and J.B.R.; visualization—R.S. and T.O.A.; writing original draft—R.S., C.C.P., A.F.A., C.B., B.R., I.S.M., T.S., I.M.P., and J.B.R.; writing review and editing—R.S., T.O.A., and J.B.R.

DECLARATION OF INTERESTS

The authors declare no conflict of interest.

INCLUSION AND DIVERSITY

We support inclusive, diverse, and equitable conduct of research.

Received: February 15, 2023
Revised: August 14, 2023
Accepted: October 31, 2023
Published: November 18, 2023

REFERENCES

1. Croese, T., Castellani, G., and Schwartz, M. (2021). Immune cell compartmentalization for brain surveillance and protection. Nat. Immunol. *22*, 1083–1092.
2. Davalos, D., Grutzendler, J., Yang, G., Kim, J.V., Zuo, Y., Jung, S., Littman, D.R., Dustin, M.L., and Gan, W.-B. (2005). ATP mediates rapid microglial response to local brain injury in vivo. Nat. Neurosci. *8*, 752–758.
3. Nimmerjahn, A., Kirchhoff, F., and Helmchen, F. (2005). Resting Microglial Cells Are Highly Dynamic Surveillants of Brain Parenchyma in Vivo. Science *308*, 1314–1318.
4. Bernier, L.P., Bohlen, C.J., York, E.M., Choi, H.B., Kamyabi, A., Dissing-Olesen, L., Hefendehl, J.K., Collins, H.Y., Stevens, B., Barres, B.A., and MacVicar, B.A. (2019). Nanoscale Surveillance of the Brain by Microglia via cAMP-Regulated Filopodia. Cell Rep. *27*, 2895–2908.e4.
5. Nguyen, P.T., Dorman, L.C., Pan, S., Vainchtein, I.D., Han, R.T., Nakao-Inoue, H., Taloma, S.E., Barron, J.J., Molofsky, A.B., Kheirbek, M.A., and Molofsky, A.V. (2020). Microglial Remodeling of the Extracellular Matrix Promotes Synapse Plasticity. Cell *182*, 388–403.e15.
6. Parkhurst, C.N., Yang, G., Ninan, I., Savas, J.N., Yates, J.R., 3rd, Lafaille, J.J., Hempstead, B.L., Littman, D.R., and Gan, W.B. (2013). Microglia promote learning-dependent synapse formation through brain-derived neurotrophic factor. Cell *155*, 1596–1609.
7. Socodato, R., Portugal, C.C., Canedo, T., Rodrigues, A., Almeida, T.O., Henriques, J.F., Vaz, S.H., Magalhães, J., Silva, C.M., Baptista, F.I., et al. (2020). Microglia Dysfunction Caused by the Loss of Rhoa Disrupts Neuronal Physiology and Leads to Neurodegeneration. Cell Rep. *31*, 107796.
8. Ndoja, A., Reja, R., Lee, S.-H., Webster, J.D., Ngu, H., Rose, C.M., Kirkpatrick, D.S., Modrusan, Z., Chen, Y.-J.J., Dugger, D.L., et al. (2020). Ubiquitin Ligase COP1 Suppresses Neuroinflammation by Degrading c/EBPβ in Microglia. Cell *182*, 1156–1169.e12.
9. Cserép, C., Pósfai, B., and Dénes, Á. (2021). Shaping Neuronal Fate: Functional Heterogeneity of Direct Microglia-Neuron Interactions. Neuron *109*, 222–240.
10. Mayford, M., Siegelbaum, S.A., and Kandel, E.R. (2012). Synapses and memory storage. Cold Spring Harb. Perspect. Biol. *4*, a005751.
11. Hall, A., and Lalli, G. (2010). Rho and Ras GTPases in axon growth, guidance, and branching. Cold Spring Harb. Perspect. Biol. *2*, a001818.
12. Thurnherr, T., Benninger, Y., Wu, X., Chrostek, A., Krause, S.M., Nave, K.-A., Franklin, R.J.M., Brakebusch, C., Suter, U., and Relvas, J.B. (2006). Cdc42 and Rac1 Signaling Are Both Required for and Act Synergistically in the Correct Formation of Myelin Sheaths in the CNS. J. Neurosci. *26*, 10110–10119.
13. Zeug, A., Müller, F.E., Anders, S., Herde, M.K., Minge, D., Ponimaskin, E., and Henneberger, C. (2018). Control of astrocyte morphology by Rho GTPases. Brain Res. Bull. *136*, 44–53.
14. Afshordel, S., Wood, W.G., Igbavboa, U., Muller, W.E., and Eckert, G.P. (2014). Impaired geranylgeranyltransferase-I regulation reduces membrane-associated Rho protein levels in aged mouse brain. J. Neurochem. *129*, 732–742.
15. Kikuchi, M., Sekiya, M., Hara, N., Miyashita, A., Kuwano, R., Ikeuchi, T., Iijima, K.M., and Nakaya, A. (2020). Disruption of a RAC1-centred network is associated with Alzheimer's disease pathology and causes age-dependent neurodegeneration. Hum. Mol. Genet. *29*, 817–833.
16. Rong, Z., Cheng, B., Zhong, L., Ye, X., Li, X., Jia, L., Li, Y., Shue, F., Wang, N., Cheng, Y., et al. (2020). Activation of FAK/Rac1/Cdc42-GTPase signaling ameliorates impaired microglial migration response to Aβ42 in triggering receptor expressed on myeloid cells 2 loss-of-function murine models. Faseb. J. *34*, 10984–10997.
17. Goldmann, T., Wieghofer, P., Müller, P.F., Wolf, Y., Varol, D., Yona, S., Brendecke, S.M., Kierdorf, K., Staszewski, O., Datta, M., et al. (2013). A new type of microglia gene targeting shows TAK1 to be pivotal in CNS autoimmune inflammation. Nat. Neurosci. *16*, 1618–1626.
18. Yona, S., Kim, K.W., Wolf, Y., Mildner, A., Varol, D., Breker, M., Strauss-Ayali, D., Viukov, S., Guilliams, M., Misharin, A., et al. (2013). Fate mapping reveals origins and dynamics of monocytes and tissue macrophages under homeostasis. Immunity *38*, 79–91.
19. Chrostek, A., Wu, X., Quondamatteo, F., Hu, R., Sanecka, A., Niemann, C., Langbein, L., Haase, I., and Brakebusch, C. (2006). Rac1 is crucial for hair follicle integrity but is not essential for maintenance of the epidermis. Mol. Cell Biol. *26*, 6957–6970.
20. Sahasrabuddhe, V., and Ghosh, H.S. (2022). Cx3Cr1-Cre induction leads to microglial activation and IFN-1 signaling caused by DNA damage in early postnatal brain. Cell Rep. *38*, 110252.
21. Goldmann, T., Wieghofer, P., Jordão, M.J.C., Prutek, F., Hagemeyer, N., Frenzel, K., Amann, L., Staszewski, O., Kierdorf, K., Krueger, M., et al. (2016). Origin, fate and dynamics of macrophages at central nervous system interfaces. Nat. Immunol. *17*, 797–805.

22. Castellano, F., Montcourrier, P., and Chavrier, P. (2000). Membrane recruitment of Rac1 triggers phagocytosis. J. Cell Sci. *113*, 2955–2961.

23. Caron, E., and Hall, A. (1998). Identification of Two Distinct Mechanisms of Phagocytosis Controlled by Different Rho GTPases. Science *282*, 1717–1721.

24. Massol, P., Montcourrier, P., Guillemot, J.-C., and Chavrier, P. (1998). Fc receptor-mediated phagocytosis requires CDC42 and Rac1. EMBO J. *17*, 6219–6229.

25. Cox, D., Chang, P., Zhang, Q., Reddy, P.G., Bokoch, G.M., and Greenberg, S. (1997). Requirements for Both Rac1 and Cdc42 in Membrane Ruffling and Phagocytosis in Leukocytes. J. Exp. Med. *186*, 1487–1494.

26. Werner, E. (2004). GTPases and reactive oxygen species: switches for killing and signaling. J. Cell Sci. *117*, 143–153.

27. Hordijk, P.L. (2006). Regulation of NADPH oxidases: the role of Rac proteins. Circ. Res. *98*, 453–462.

28. Ayata, P., Badimon, A., Strasburger, H.J., Duff, M.K., Montgomery, S.E., Loh, Y.H.E., Ebert, A., Pimenova, A.A., Ramirez, B.R., Chan, A.T., et al. (2018). Epigenetic regulation of brain region-specific microglia clearance activity. Nat. Neurosci. *21*, 1049–1060.

29. A-Gonzalez, N., Quintana, J.A., García-Silva, S., Mazariegos, M., González de la Aleja, A., Nicolás-Ávila, J.A., Walter, W., Adrover, J.M., Crainiciuc, G., Kuchroo, V.K., et al. (2017). Phagocytosis imprints heterogeneity in tissue-resident macrophages. J. Exp. Med. *214*, 1281–1296.

30. Stephan, A.H., Barres, B.A., and Stevens, B. (2012). The Complement System: An Unexpected Role in Synaptic Pruning During Development and Disease. Annu. Rev. Neurosci. *35*, 369–389.

31. Mendiola, A.S., Ryu, J.K., Bardehle, S., Meyer-Franke, A., Ang, K.K.H., Wilson, C., Baeten, K.M., Hanspers, K., Merlini, M., Thomas, S., et al. (2020). Transcriptional profiling and therapeutic targeting of oxidative stress in neuroinflammation. Nat. Immunol. *21*, 513–524.

32. Pal, R., Basu Thakur, P., Li, S., Minard, C., and Rodney, G.G. (2013). Real-time imaging of NADPH oxidase activity in living cells using a novel fluorescent protein reporter. PLoS One *8*, e63989.

33. Sousa, C., Golebiewska, A., Poovathingal, S.K., Kaoma, T., Pires-Afonso, Y., Martina, S., Coowar, D., Azuaje, F., Skupin, A., Balling, R., et al. (2018). Single-cell transcriptomics reveals distinct inflammation-induced microglia signatures. EMBO Rep. *19*, e46171.

34. Keren-Shaul, H., Spinrad, A., Weiner, A., Matcovitch-Natan, O., Dvir-Szternfeld, R., Ulland, T.K., David, E., Baruch, K., Lara-Astaiso, D., Toth, B., et al. (2017). A Unique Microglia Type Associated with Restricting Development of Alzheimer's Disease. Cell *169*, 1276–1290.e17.

35. Hammond, T.R., Dufort, C., Dissing-Olesen, L., Giera, S., Young, A., Wysoker, A., Walker, A.J., Gergits, F., Segel, M., Nemesh, J., et al. (2019). Single-Cell RNA Sequencing of Microglia throughout the Mouse Lifespan and in the Injured Brain Reveals Complex Cell-State Changes. Immunity *50*, 253–271.e6.

36. Socodato, R., Portugal, C.C., Rodrigues, A., Henriques, J., Rodrigues, C., Figueira, C., and Relvas, J.B. (2018). Redox tuning of Ca(2+) signaling in microglia drives glutamate release during hypoxia. Free Radic. Biol. Med. *118*, 137–149.

37. Socodato, R., Henriques, J.F., Portugal, C.C., Almeida, T.O., Tedim-Moreira, J., Alves, R.L., Canedo, T., Silva, C., Magalhães, A., Summavielle, T., and Relvas, J.B. (2020). Daily alcohol intake triggers aberrant synaptic pruning leading to synapse loss and anxiety-like behavior. Sci. Signal. *13*, eaba5754.

38. Canedo, T., Portugal, C.C., Socodato, R., Almeida, T.O., Terceiro, A.F., Bravo, J., Silva, A.I., Magalhães, J.D., Guerra-Gomes, S., Oliveira, J.F., et al. (2021). Astrocyte-derived TNF and glutamate critically modulate microglia activation by methamphetamine. Neuropsychopharmacology *46*, 2358–2370.

39. Sato, M., Ueda, Y., and Umezawa, Y. (2006). Imaging diacylglycerol dynamics at organelle membranes. Nat. Methods *3*, 797–799.

40. Palmer, A.E., Jin, C., Reed, J.C., and Tsien, R.Y. (2004). Bcl-2-mediated alterations in endoplasmic reticulum Ca^{2+} analyzed with an improved genetically encoded fluorescent sensor. Proc. Natl. Acad. Sci. USA *101*, 17404–17409.

41. Wu, J., Liu, L., Matsuda, T., Zhao, Y., Rebane, A., Drobizhev, M., Chang, Y.F., Araki, S., Arai, Y., March, K., et al. (2013). Improved orange and red $Ca^{2}\pm$ indicators and photophysical considerations for optogenetic applications. ACS Chem. Neurosci. *4*, 963–972.

42. Violin, J.D., Zhang, J., Tsien, R.Y., and Newton, A.C. (2003). A genetically encoded fluorescent reporter reveals oscillatory phosphorylation by protein kinase C. J. Cell Biol. *161*, 899–909.

43. Fu, M., and Zuo, Y. (2011). Experience-dependent structural plasticity in the cortex. Trends Neurosci. *34*, 177–187.

44. Woolfrey, K.M., and Dell'Acqua, M.L. (2015). Coordination of Protein Phosphorylation and Dephosphorylation in Synaptic Plasticity. J. Biol. Chem. *290*, 28604–28612.

45. Chen, T.W., Wardill, T.J., Sun, Y., Pulver, S.R., Renninger, S.L., Baohan, A., Schreiter, E.R., Kerr, R.A., Orger, M.B., Jayaraman, V., et al. (2013). Ultrasensitive fluorescent proteins for imaging neuronal activity. Nature *499*, 295–300.

46. Whitelaw, B.S., Stoessel, M.B., and Majewska, A.K. (2023). Movers and shakers: microglial dynamics and modulation of neural networks. Glia *71*, 1575–1591.

47. Bibb, J.A., Mayford, M.R., Tsien, J.Z., and Alberini, C.M. (2010). Cognition Enhancement Strategies. J. Neurosci. *30*, 14987–14992.

48. Ögren, S.O., and Stiedl, O. (2010). Passive Avoidance. In Encyclopedia of Psychopharmacology, I.P. Stolerman, ed. (Springer Berlin Heidelberg), pp. 960–967.

49. Lueptow, L.M. (2017). Novel Object Recognition Test for the Investigation of Learning and Memory in Mice. JoVE, e55718.

50. Kraeuter, A.K., Guest, P.C., and Sarnyai, Z. (2019). The Y-Maze for Assessment of Spatial Working and Reference Memory in Mice. Methods Mol. Biol. *1916*, 105–111.

51. Kaidanovich-Beilin, O., Lipina, T., Vukobradovic, I., Roder, J., and Woodgett, J.R. (2011). Assessment of social interaction behaviors. J. Vis. Exp., e2473.

52. Zhou, X., and Zheng, Y. (2013). Cell type-specific signaling function of RhoA GTPase: lessons from mouse gene targeting. J. Biol. Chem. *288*, 36179–36188.

53. Pick, E. (2014). Role of the Rho GTPase Rac in the activation of the phagocyte NADPH oxidase: outsourcing a key task. Small GTPases *5*, e27952.

54. Zhao, X., Carnevale, K.A., and Cathcart, M.K. (2003). Human monocytes use Rac1, not Rac2, in the NADPH oxidase complex. J. Biol. Chem. *278*, 40788–40792.

55. Hong, S., and Stevens, B. (2016). Microglia: Phagocytosing to Clear, Sculpt, and Eliminate. Dev. Cell *38*, 126–128.

56. Holt, C.E., Martin, K.C., and Schuman, E.M. (2019). Local translation in neurons: visualization and function. Nat. Struct. Mol. Biol. *26*, 557–566.

57. Domnauer, M., Zheng, F., Li, L., Zhang, Y., Chang, C.E., Unruh, J.R., Conkright-Fincham, J., McCroskey, S., Florens, L., Zhang, Y., et al. (2021). Proteome plasticity in response to persistent environmental change. Mol. Cell *81*, 3294–3309.e12.

58. Cajigas, I.J., Tushev, G., Will, T.J., tom Dieck, S., Fuerst, N., and Schuman, E.M. (2012). The local transcriptome in the synaptic neuropil revealed by deep sequencing and high-resolution imaging. Neuron *74*, 453–466.

59. Irala, D., Bonafina, A., Fontanet, P.A., Alsina, F.C., Paratcha, G., and Ledda, F. (2016). The GDNF-GFRα1 complex promotes the development of hippocampal dendritic arbors and spines via NCAM. Development *143*, 4224–4235.

60. Dityatev, A., Dityateva, G., and Schachner, M. (2000). Synaptic Strength as a Function of Post- versus Presynaptic Expression of the Neural Cell Adhesion Molecule NCAM. Neuron *26*, 207–217.

61. Arami, S., Jucker, M., Schachner, M., and Welzl, H. (1996). The effect of continuous intraventricular infusion of L1 and NCAM antibodies on spatial learning in rats. Behav. Brain Res. *81*, 81–87.

62. Sytnyk, V., Leshchyns'ka, I., Nikonenko, A.G., and Schachner, M. (2006). NCAM promotes assembly and activity-dependent remodeling of the postsynaptic signaling complex. J. Cell Biol. *174*, 1071–1085.

63. Peng, J., Liu, Y., Umpierre, A.D., Xie, M., Tian, D.S., Richardson, J.R., and Wu, L.J. (2019). Microglial P2Y12 receptor regulates ventral hippocampal CA1 neuronal excitability and innate fear in mice. Mol. Brain *12*, 71.

64. Voet, S., Mc Guire, C., Hagemeyer, N., Martens, A., Schroeder, A., Wieghofer, P., Daems, C., Staszewski, O., Vande Walle, L., Jordao, M.J.C., et al. (2018). A20 critically controls microglia activation and inhibits inflammasome-dependent neuroinflammation. Nat. Commun. *9*, 2036.

65. Gubert, C., and Hannan, A.J. (2019). Environmental enrichment as an experience-dependent modulator of social plasticity and cognition. Brain Res. *1717*, 1–14.

66. Karabiyik, C., Fernandes, R., Figueiredo, F.R., Socodato, R., Brakebusch, C., Lambertsen, K.L., Relvas, J.B., and Santos, S.D. (2018). Neuronal Rho GTPase Rac1 elimination confers neuroprotection in a mouse model of permanent ischemic stroke. Brain Pathol. *28*, 569–580.

67. Schindelin, J., Arganda-Carreras, I., Frise, E., Kaynig, V., Longair, M., Pietzsch, T., Preibisch, S., Rueden, C., Saalfeld, S., Schmid, B., et al. (2012). Fiji: an open-source platform for biological-image analysis. Nat. Methods *9*, 676–682.

68. Socodato, R., Melo, P., Ferraz-Nogueira, J.P., Portugal, C.C., and Relvas, J.B. (2020). A Protocol for FRET-Based Live-Cell Imaging in Microglia. STAR Protoc. *1*, 100147.

69. Portugal, C.C., Socodato, R., Canedo, T., Silva, C.M., Martins, T., Correixas, V.S.M., Loiola, E.C., Gess, B., Röhr, D., Santiago, A.R., et al. (2017). Caveolin-1-mediated internalization of the vitamin C transporter SVCT2 in microglia triggers an inflammatory phenotype. Sci. Signal. *10*, eaal2005.

70. Friard, O., and Gamba, M. (2016). BORIS: a free, versatile open-source event-logging software for video/audio coding and live observations. Methods Ecol. Evol. *7*, 1325–1330.

71. Liao, Y., Wang, J., Jaehnig, E.J., Shi, Z., and Zhang, B. (2019). WebGestalt 2019: gene set analysis toolkit with revamped UIs and APIs. Nucleic Acids Res. *47*, W199–W205.

72. Szklarczyk, D., Gable, A.L., Lyon, D., Junge, A., Wyder, S., Huerta-Cepas, J., Simonovic, M., Doncheva, N.T., Morris, J.H., Bork, P., et al. (2019). STRING v11: protein-protein association networks with increased coverage, supporting functional discovery in genome-wide experimental datasets. Nucleic Acids Res. *47*, D607–D613.

73. Hornbeck, P.V., Zhang, B., Murray, B., Kornhauser, J.M., Latham, V., and Skrzypek, E. (2015). PhosphoSitePlus, 2014: mutations, PTMs and recalibrations. Nucleic Acids Res. *43*, D512–D520.

74. Horn, H., Schoof, E.M., Kim, J., Robin, X., Miller, M.L., Diella, F., Palma, A., Cesareni, G., Jensen, L.J., and Linding, R. (2014). KinomeXplorer: an integrated platform for kinome biology studies. Nat. Methods *11*, 603–604.

75. Betts, M.J., Lu, Q., Jiang, Y., Drusko, A., Wichmann, O., Utz, M., Valtierra-Gutiérrez, I.A., Schlesner, M., Jaeger, N., Jones, D.T., et al. (2015). Mechismo: predicting the mechanistic impact of mutations and modifications on molecular interactions. Nucleic Acids Res. *43*, e10.

76. Merico, D., Isserlin, R., Stueker, O., Emili, A., and Bader, G.D. (2010). Enrichment Map: A Network-Based Method for Gene-Set Enrichment Visualization and Interpretation. PLoS One *5*, e13984.

77. Legeay, M., Doncheva, N.T., Morris, J.H., and Jensen, L.J. (2020). Visualize omics data on networks with Omics Visualizer. F1000Res. *9*, 157.

78. Gonzalez-Lozano, M.A., Koopmans, F., Sullivan, P.F., Protze, J., Krause, G., Verhage, M., Li, K.W., Liu, F., and Smit, A.B. (2020). Stitching the synapse: Cross-linking mass spectrometry into resolving synaptic protein interactions. Sci. Adv. *6*, eaax5783.

STAR★METHODS

KEY RESOURCES TABLE

REAGENT or RESOURCE	SOURCE	IDENTIFIER
Antibodies		
Rac1 antibody [0.T.127]	Abcam	Cat# ab33186, RRID:AB_777598
Iba1	Wako	Cat# 019–19741, RRID:AB_839504
CD11b clone M1/70.15	BD Biosciences	Cat# MA1-045, RRID:AB_325399
PSD95 clone 6G6-1C9	Thermo Fisher Scientific	Cat# MA1-045, RRID:AB_325399
Anti-PSD95	Synaptic Systems	Cat# 124 308, RRID:AB_2905564
CD68 clone FA-11	Bio-Rad	Cat# MCA1957T, RRID:AB_2074849
Fc Receptor Blocking Solution	BioLegend	Cat# 156603, RRID:AB_2783137
NeuN	Millipore	Cat# MAB377, RRID:AB_2298772
APC anti-mouse/human CD11b antibody	BioLegend	Cat# 101212, RRID:AB_312795
Alexa Fluor® 647 anti-mouse/human CD11b antibody	BioLegend	Cat# 101218, RRID: AB_389327
PE anti-mouse CD45 antibody	BioLegend	Cat# 103106, RRID:AB_312971
PerCP/Cy5.5 anti-mouse Ly6C antibody	BioLegend	Cat# 128012, RRID:AB_1659241
BV421 anti-mouse MHC-II antibody	BioLegend	Cat# 107631, RRID:AB_10900075
PE/Cy7 anti-mouse Annexin-V antibody	BioLegend	Cat# 640950
PE/Cy7 anti-mouse Ki67 antibody	BioLegend	Cat# 652425, RRID:AB_2632693
CaMKII (pan) (D11A10) Rabbit mAb	Cell Signaling Technology	Cat# 4436, RRID:AB_10545451
Phospho-CaMKII (Thr286) (D21E4) Rabbit mAb	Cell Signaling Technology	Cat# 12716, RRID:AB_2713889
Mouse Anti-Glyceraldehyde-3-Phosphate Dehydrogenase (GAPDH) Antibody, Unconjugated	HyTest	Cat# 5G4-9B3, RRID:AB_1616725
Peroxidase-AffiniPure Donkey Anti-Rabbit IgG (H + L)	Jackson ImmunoResearch Labs	Cat# 711-035-152, RRID:AB_10015282
Peroxidase-AffiniPure Goat Anti-Mouse IgG (H + L)	Jackson ImmunoResearch Labs	Cat# 115-035-146, RRID:AB_2307392
CD11b MicroBeads, human and mouse	Miltenyi Biotech	Cat# 130-049-601, RRID:AB_2927377
Myelin Removal Beads II, human, mouse, rat	Miltenyi Biotech	Cat# 130-096-733
MojoSort™ Mouse P2RY12 Selection Kit	BioLegend	Cat# 480114
Goat anti-Mouse IgG (H + L) Cross-Adsorbed Secondary Antibody, Alexa Fluor™ 488	Thermo Fisher Scientific	Cat# A-11001, RRID:AB_2534069
Goat anti-Mouse IgG (H + L) Cross-Adsorbed Secondary Antibody, Alexa Fluor™ 568	Thermo Fisher Scientific	Cat# A-11004, RRID:AB_2534072
Goat anti-Rabbit IgG (H + L) Cross-Adsorbed Secondary Antibody, Alexa Fluor™ 568	Thermo Fisher Scientific	Cat# A-11011, RRID:AB_143157
Goat anti-Rat IgG (H + L) Cross-Adsorbed Secondary Antibody, Alexa Fluor™ 568	Thermo Fisher Scientific	Cat# A-11077, RRID:AB_2534121
Goat anti-Mouse IgG (H + L) Highly Cross-Adsorbed Secondary Antibody, Alexa Fluor™ Plus 647	Thermo Fisher Scientific	Cat# A32728, RRID:AB_2633277
Goat anti-Rabbit IgG (H + L) Cross-Adsorbed Secondary Antibody, Alexa Fluor™ 647	Thermo Fisher Scientific	Cat# A-21244, RRID:AB_2535812
Goat Anti-Guinea Pig IgG (H + L) Highly Cross-adsorbed Antibody, Alexa Fluor 647 Conjugated	Thermo Fisher Scientific	Cat# A-21450, RRID:AB_141882
Chemicals, peptides, and recombinant proteins		
Tamoxifen	Merck	Cat# T5648
Recombinant Murine GM-CSF	Peprotech	Cat# 315-03
Adenosine 5′-triphosphate disodium salt hydrate	Merck	Cat# A3377
L-α-Phosphatidylcholine	Merck	Cat# P3782

(*Continued on next page*)

Continued

REAGENT or RESOURCE	SOURCE	IDENTIFIER
Dihydroethidium	Merck	Cat# D7008
Critical commercial assays		
Zombie Violet Fixable Viability Kit	BioLegend	Cat #423114
SuperSignal™ West Pico PLUS Chemiluminescent Substrate	Thermo Fisher Scientific	Cat #34580
Permeabilization buffer	Thermo Fisher Scientific	Cat# 00-8333-56
RNeasy Plus Micro Kit	Qiagen	Cat# 74034
Agilent TapeStation High Sensitivity tape	Agilent	Cat# 5067- 5584
SuperScript® III First-Strand Synthesis SuperMix	Thermo Fisher Scientific	Cat# 18080400
iQ™ SYBR® Green Supermix	Bio-Rad	Cat# 1708880
Titanium dioxide beads	Thermo Fisher Scientific	Cat# A32993
Ion AmpliSeq™ Transcriptome Mouse Gene Expression Kit	Thermo Fisher Scientific	Cat# A36553
Deposited data		
RNA-seq	This paper	https://www.ncbi.nlm.nih.gov/geo/query/acc.cgi?acc=GSE244773
Phosphoproteomics	This paper	https://ftp.pride.ebi.ac.uk/pride/data/archive/2023/10/PXD045719/
Experimental models: Cell lines		
HMC3	ATCC	Cat# CRL-3304, RRID:CVCL_II76
Experimental models: Organisms/strains		
Mouse: $Rac1^{fl/fl}$:$Cx3cr1^{CreER+}$	This paper	N/A
Mouse: B6.129P2(Cg)-$Cx3cr1^{tm2.1(cre/ERT2)Litt}$/WganJ (herein $Cx3cr1^{CreER-EYFP}$)	The Jackson Laboratory	Cat# JAX:021160; RRID:IMSR_JAX:021160
Mouse: $Rac1^{tm1Brak}$ (herein $Rac1^{fl/fl}$)	MGI	RRID:MGI:3665264
Oligonucleotides		
Primers in Table S11	This paper	N/A
Recombinant DNA		
Daglas-pm1	Sato et al.[39]	N/A
pcDNA-D1ER	Palmer et al.[40]	Addgene #36325
CMV-R-GECO1	Wu et al.[41]	Addgene #32444
CKAR	Violin et al.[42]	Addgene #14860
GFP.Cre	Gift from Tyler Jacks	Addgene #20781
p47-roGFP	Pal et al.[32]	N/A
pLKO-empty	Karabiyik et al.[66]	N/A
pLKO-Rac1 shRNA	Karabiyik et al.[66]	N/A
scrambled-mCherry shRNA control	Karabiyik et al.[66]	N/A
mCherry-Rac1 shRNA	Karabiyik et al.[66]	N/A
pRK5-myc-Rac1-wt	Gift from Gary Bokoch	Addgene #12985
pRK5-myc-Rac1-T17N	Gift from Gary Bokoch	Addgene #12984
pGP-CMV-GCaMP6f	Chen et al.[45]	Addgene #40755
mCherry-Lifeact-7	Gift from Michael Davidson	Addgene #54491
Software and algorithms		
Fiji	Schindelin et al.[67]	RRID:SCR_002285
Transcriptome Analysis Console	Thermo Fisher Scientific	RRID:SCR_016519
Proteome Discoverer	Thermo Fisher Scientific	RRID:SCR_014477
GraphPad Prism	GraphPad Software	RRID:SCR_002798
Adobe Illustrator	Adobe	RRID:SCR_010279
Imaris	Oxford Instruments	RRID:SCR_007370

(*Continued on next page*)

Continued

REAGENT or RESOURCE	SOURCE	IDENTIFIER
Image Lab Software	Bio-Rad	RRID:SCR_014210
FlowJo	BD Biosciences	RRID:SCR_008520
Torrent Suite v5.12	Thermo Fisher Scientific	N/A
Python 3.8.5	Python Software Foundation	RRID: SCR_008394
Other		
Novel object recognition apparatus	This paper (custom made)	N/A
Step-down passive avoidance apparatus	This paper (custom made)	N/A
Three chamber sociability apparatus	This paper (custom made)	N/A
Y-maze apparatus	This paper (custom made)	N/A
OCT embedding medium	Thermo Fisher Scientific	Cat # 6769006
Leica CM3050S Cryostat	Leica Biosystems	RRID:SCR_020214
Leica TCS SP8 confocal microscope	Leica Microsystems	https://www.ppbi.pt/joomla30/index.php/i3s-alm/24-nodes/equipment/156-equipment-ibmc
FACS Canto II analyzer	BS Biosciences	RRID:SCR_018056
U bottom 96-well plate	Falcon	Cat# 351177
Bioanalyzer 2100 RNA Pico chips	Agilent	Cat# 5067-1513
Ion Chef Instrument	Thermo Fisher Scientific	Cat# 4484177
Ion S5XL™ sequencer	Thermo Fisher Scientific	Cat# A27213
iQ™5 multicolor real-time PCR detection system	Bio-Rad	RRID:SCR_019721
Ultimate 3000 liquid chromatography system	Thermo Fisher Scientific	https://www.i3s.up.pt/scientific-platform.php?groupid=56#Resources
Q-Exactive Hybrid Quadrupole-Orbitrap mass spectrometer	Thermo Fisher Scientific	https://www.i3s.up.pt/scientific-platform.php?groupid=56#Resources
Leica DMI6000B inverted microscope	Leica Microsystems	https://www.ppbi.pt/joomla30/index.php/i3s-alm/24-nodes/equipment/156-equipment-ibmc

RESOURCE AVAILABILITY

Lead contact

Further information and requests for resources and reagents should be directed to and will be fulfilled by the Lead Contact, João Relvas (jrelvas@ibmc.up.pt).

Materials availability

This study did not generate new unique reagents.

Data and code availability

- RNA-seq and Phosphoproteomics data have been deposited at GEO and PRIDE, respectively. The data is publicly available as of the publication date, and the accession numbers are listed in the key resources table. Other data generated in this study is available from the lead contact upon request.
- This paper does not report any original code.
- Any additional information required to reanalyze the data reported in this paper is available from the lead contact upon reasonable request.

EXPERIMENTAL MODEL AND STUDY PARTICIPANT DETAILS

Animals

All mice experiments were reviewed by i3S animal ethical committee and were approved by Direção-Geral de Alimentação e Veterinária (DGAV). Animals were maintained with an inverted 12h/12h light-dark cycle and were allowed free access to food and water. Mice were housed under standardized cages and specific pathogen-free conditions. Experiments were carried out following the 3Rs ethics policy.

Conditional Rac1-deficient mice

Cx3cr1$^{CreER-EYFP}$ mice were purchased from Jackson Laboratories and used as before.[7] In such mice, the *Cx3cr1* promoter drives high expression of the CreER cassette in microglia.[6] Mice homozygous for the *Rac1* floxed allele[19] were backcrossed for at least ten generations and were kept at the I3S animal facility. PCR determined all genotypes on genomic DNA. Rac1 floxed mice were crossed with Cx3cr1$^{CreER-EYFP}$ mice. Progeny of interest were: Controls (Rac1$^{fl/fl}$ or Cx3cr1^{CreER+}) and mutants (Rac1$^{fl/fl}$:Cx3cr1^{CreER+}). Mice (4/5-weeks-old) were given tamoxifen (5 mg *per* animal by oral gavage; 1 mg daily for five days) and then analyzed post-tamoxifen. Experiments were performed in female and male mice, all kept on a C57BL/6 background.

Microglial cell line

The human microglial cell line HMC3 was obtained from ATCC (ATCC CRL-3304). HMC3 microglia were plated on plastic-bottom culture dishes (μ-Dish 35 mm, iBidi) and transfected, as before,[68] with different biosensors. Cells were cultivated and maintained as before (Socodato et al., 2020a; Socodato et al., 2020b; Socodato et al., 2020c).

Primary microglial cultures

Primary cultures of cortical microglia were prepared as before.[38,69] Briefly, cerebral cortices from Wistar pups (P0 to P2) were dissected and digested with trypsin-EDTA in the presence of DNase for 15 min (37°C). Cells were seeded in DMEM Glutamax-I medium supplemented with 10% Fetal Bovine Serum (FBS) and 1% Penicillin/Streptomycin. Cultures were kept at 37°C and 95% air/5% CO_2 in a humidified incubator. Flasks were shaked orbitally (200rpm for 2h) to detach microglia and obtain purified microglial cultures. CD11b labeling showed a purity of >95%.

Primary cultures of cortical neurons

Brain cortices were dissected from embryonic day 18 Wistar rat embryos and dissociated using trypsin (0.25%, v/v). Neurons were plated at a final density of 1×10^4 to 5×10^4 cells per dish and cultured in the presence of a glial feeder layer. Cells were cultured in phenol red-free Neurobasal medium supplemented with B27 supplement (1:50, v/v), 25 mM glutamate, 0.5 mM glutamine, and gentamicin (0.12 mg/mL). To prevent glial overgrowth, neuronal cultures were treated with 5 mM cytosine arabinoside after 3 days *in vitro* and maintained in a humidified incubator with 5% CO_2/95% air at 37°C for up to 2 weeks, feeding the cells once per week by replacing one-third of the medium.

METHOD DETAILS

Environmental enrichment protocol

Mice with 4–5 weeks of age were weighted and placed in Type III cages for three days with two different housing conditions: control environment (CE) and enriched environment (EE). Littermates were randomly assigned to one of the housing conditions, with Rac1$^{fl/fl}$ and Cx3cr1^{CreER+}:Rac1$^{fl/fl}$ mice in every cage. CE only contained bedding material (corn cob, grade 12) and tissue paper. EE had bedding material, tissue paper, a small cardboard tube, four small aspen bricks, a wood ladder, a vertical plastic running wheel with a steep metal grid, a dome home, a plastic Lego-like block, and sunflower seeds. Mice were weighted immediately before tamoxifen administration and then weighted once per week during home-cage change for the first three weeks after tamoxifen administration. Mice were kept in the same housing conditions until the end of the protocol (18 weeks) with access to food and water *ad libitum*. Home cages in CE and EE conditions were changed weekly. Enrichment material was checked every week: new tissue paper and sunflower seeds were added weekly, while cardboard tubes, dome homes, and aspen bricks were replaced when destroyed or highly degraded. The remaining enrichment material was constantly transferred to the new cage during weekly home-cage changes. The spatial organization of the enrichment material was maintained throughout the experiment. Manipulation of mice during the behavioral test period was reduced to the minimum necessary.

Behavioral tests

Procedures were conducted in the dark phase of the light/dark cycle and performed blind to genotypes. The order and interval between tests were used as acclimation for the next test and performed in the following order: (1) three-chamber sociability; (2) novel object recognition; (3) Y-maze; (4) step-down passive avoidance. The experimenter recording the behavioral parameters during test sections was blind to genotypes.

Three-chamber sociability

Mice were first habituated to the empty apparatus, a three-chamber box consisting of three interconnected lined compartments, for 10 min. After the habituation phase, mice were tested in the sociability task. In this phase, subject mice socialize with a conspecific mouse in a cage or explore an empty cage in opposite external compartments. All phases during 10 min and the placement of stranger mice on the left or right side of the chamber are systematically altered between trials. The time spent in each compartment (four paws have entered the chamber) and the exploration time (direct contact or stretching in 3–5 cm around the mouse or empty cage) were measured. All parameters were evaluated by Boris software.[70] Because female control mice did not significantly enhance sociability parameters, only male mice (both genotypes) were used in this test.

Object recognition (NOR)

The NOR test used experimental procedures similar to the three-chamber test. The test consists of three phases. During the habituation phase, mice can explore the apparatus for 10 min (used to perform habituation in three-chamber test, 24 h before). The next day, during the object familiarization/acquisition phase, two identical objects were placed at the center of each outer chamber. Mice were allowed to explore the objects for 10 min freely. Then mice were returned to their home cage, and after 4 h (inter-trial interval, ITI), the retention phase was performed. In this phase, one of the familiar objects is changed by a novel object, and animals are allowed to explore these objects for 3 min. Exploration was defined as follows: the mouse touched the object with its nose, or the mouse's nose was directed toward the object at a distance shorter than 2 cm. The discrimination index (DI) was calculated as before[7] and used as an index of memory function, DI = (time exploring the novel object)/(total time spent exploring both objects). All parameters were evaluated by Boris software.[70]

Y-maze

Wrong arm returns (# errors), a measure of spatial working memory, were assessed by allowing mice to explore all three arms of the maze, motivated by an innate interest of rodents to explore previously unvisited areas. The mice are positioned in the center of the apparatus and allowed to explore freely for 8 min. During the test, visual clues were placed on the walls. Entries in the same arm during the spontaneous alternation phase were considered wrong arm returns and used as the number of working memory errors.

Step-down passive avoidance

The step-down test was used to assess the long-term memory and consisted of two phases. First, in the training phase, each mouse was placed in the center of an elevated platform (15 mm above the grid floor), and the step-down from the platform with four paws was immediately followed by a foot shock (0.5 mA) for 2 s. The latency to step-down was measured (maximum of 120s; minimum 10 s). Afterward, the animals were presented to the retention phase 24 h after training. This phase was conducted in the absence of shock, and the step-down latency from the platform was recorded (up to 120 s) and evaluated as an indicator of memory retention.

Tissue preparation and immunofluorescence

After animal perfusion with ice-cold PBS (15 mL), brains were fixed by immersion in 4% PFA in PBS, pH 7.2 overnight. After that, brains were washed with PBS and then cryoprotected using a sucrose gradient in a row (15 and 30%). After 24 h, brains were mounted in an OCT embedding medium, frozen, and cryosectioned in the CM3050S Cryostat (Leica Biosystems). Coronal sections from brains (30 μm thickness) were collected non-sequentially on Superfrost ultra plus slides. Tissue sections from controls and experimental mice encompassing identical stereological regions were collected on the same glass slide and stored at −20°C. Frozen sections were defrosted for at least 1 h and hydrated with PBS for 15 min. Sections were permeabilized with 0.25% Triton X-100 for 15 min, washed with PBS for 10 min and blocked (5% BSA, 5% FBS, 0.1% Triton X-100) for 1 h. Primary antibodies were incubated in a blocking solution in a humidified chamber overnight at 4°C. Secondary antibodies were incubated for 2 h in a blocking solution. After the secondary antibody, sections were washed three times for 10 min with PBS. Slides were coverslipped using glycergel or Immumount.

Confocal imaging and morphometric analysis

Images from tissue sections of the neocortex and the dorsal hippocampus were acquired in 8-bit sequential mode using standard TCS mode at 400 Hz. The pinhole was kept at one airy in the Leica TCS SP8 confocal microscope. Images were illuminated with different laser combinations and resolved at 512 x 512 or 1024 x 1024 pixels format using HyD detectors, and entire z series were acquired from tissue sections. Equivalent stereological regions were obtained for all tissue sections within a given slide.

To quantify microglia (Iba1+ cells), the number of cells was manually scored, as before,[7,37] in stereological identical regions of the neocortex of stained sections (3 images per section; 3 sections per mouse for each experimental group). Statistical analyses comparing genotypes were conducted using mice as considered the experimental units; statistical significance was $p < 0.05$).

Sholl analysis was performed in ImageJ by drawing concentric circles around the microglial cell body at defined radius increments. Colocalization analyses were carried out in FIJI using the Coloc2 plugin (https://imagej.net/Coloc_2).

IMARIS Analysis

All smoothing values and rolling ball radii were empirically determined and then applied to every image. All threshold values were determined specifically for each image.

Microglia Morphological Analysis

The morphological analysis of microglia was conducted using the filaments function of the IMARIS software (version 10.1.0). Initially, all images were uploaded and pre-processed using a background subtraction filter with a rolling ball radius of 10 μm. An exaggerated surface object was subsequently created from the Ionized calcium-binding adapter molecule 1 (Iba1) channel, ensuring the inclusion of every process, using the default smoothing of 0.283 μm. This surface was utilized to mask the Iba1 channel, which facilitated the creation of the filaments object. During the creation of the filaments object, the soma diameter was adjusted to each cell and reconstructed when possible. The seed point threshold was determined for every image, and the seed points were manually classified. The segment classification option was deactivated, and no filter was applied to the segments at the end. Finally, after the filament object creation, every segment was individually verified, and any missing or incorrect segments were manually corrected and redrawn using either the auto-depth or auto-path drawing mode.

CD68 and PSD-95 Analysis

For each cell, CD68 was masked using the same microglia surface as before, and vesicles were reconstructed using the Surface object with a surface smoothing of 0.120 μm. The surfaces were filtered by volume to exclude any that were under 0.01 μm^3. After reconstruction, the vesicles were checked to ensure they were all inside the microglia being reconstructed. These surfaces were then used to mask the PSD-95 channel to calculate the volume of PSD-95 inside phagocytic vesicles. The same process was used to create the PSD-95 surfaces, but no filtering was performed this time.

PSD-95 Spots Analysis

To calculate the PSD-95 spot density, the PSD-95 channel was initially pre-processed by subtracting the background using a 1 μm rolling ball radius. A Spots object was then created using a 0.450 μm diameter with the Point Spread Function (PSF) modeling enabled and 0.900 μm elongation. The Different Spot Sizes option was also turned on using local contrast. After performing this for every image, the density was obtained using a constant Region of Interest (ROI) and dividing the number of spots in that ROI by its volume.

To calculate PSD-95-microglia contacts, the MATLAB routine 'Spots Close to Filaments' included in the software was used with the Absolute Distance option and three different distances (0.1, 0.2, and 0.3 μm).

Flow cytometry and cell sorting

Microglia were collected from the brains and other tissues of control and mutant mice using density gradient separation as before.[7,37] Single-cell suspensions (5 x 10^5 cells) were incubated with different mixes of FACS antibodies for 30 min at 4°C in the dark. Compensation settings were determined using the spleen from both the control and mutants. Cell suspensions were evaluated on a FACS Canto II analyzer (BD Immunocytometry Systems). Cell suspensions were seeded in a U bottom 96-well plate. Cells were incubated with CD45, CD11b, Ly6C, MHC-II, Annexyn-V, or Ki67. After antibody washing, for intracellular staining, cells were fixed in 2% PFA for 30 min, washed in PBS, and permeabilized with permeabilization buffer (Life Technologies 00-8333-56). Intracellular antibody staining mix was prepared in permeabilization buffer and incubated with the cells for 1 h at 4°C in the dark. After washing in permeabilization buffer, cells were incubated with Alexa Fluor 488 secondary antibody for 30 min at 25°C in the dark. After that, cells were washed twice in permeabilization buffer, resuspended in FACS staining buffer (2% BSA, 0.1% sodium azide), and analyzed in FACS Canto II. Antibody controls for Rac1 (FMO) were prepared in mixes with CD45-PE and CD11b-Alexa Fluor 647 plus secondary antibodies alone. Cell sorting was performed on a FACS ARIA cell sorter.[7] Data were analyzed by FlowJo X10 software (TreeStar).

MACS isolation of microglia

Mice (males) were perfused with ice-cold PBS, and their brains were removed. The right hemisphere was mechanically dissociated in ice-cold Dounce buffer (15mM HEPES; 0.5% Glucose; and DNAse) by six strokes in a tissue potter. Homogenate was pelleted by centrifugation, resuspended in MACS buffer (0.5% BSA; 2 mM EDTA in PBS), followed by incubation with 80 μL myelin removal microbeads. Homogenate was negatively selected using LS columns, pelleted, washed twice, resuspended in MACS buffer, and incubated 10 μL CD11b microbeads or MojoSort Mouse P2RY12 Selection Kit. $CD11b^+$ or $P2RY12^+$ fraction was selected using LS columns according to the manufacturer's instructions. Enriched fractions were centrifuged (9300 g; 1 min; 4°C) and reserved for RNA isolation or preparation of protein extracts.

RNA was isolated using the RNeasy Plus Micro Kit. RNA integrity was analyzed using the Bioanalyzer 2100 RNA Pico chips (Agilent Technologies, CA, USA).

Library preparation, Sequencing, and Bioinformatics

Ion Torrent sequencing libraries were prepared according to the AmpliSeq Library prep kit protocol as we did before.[38] Briefly, 1 ng of highly intact total RNA was reverse transcribed. The resulting cDNA was amplified for 16 cycles by adding PCR Master Mix and the AmpliSeq mouse transcriptome gene expression primer pool. Amplicons were digested with the proprietary FuPa enzyme, and then barcoded adapters were ligated onto the target amplicons. The library amplicons were bound to magnetic beads, and residual reaction components were washed off. Libraries were amplified, re-purified, and individually quantified using Agilent TapeStation High Sensitivity tape. Individual libraries were diluted to a 50 p.m. concentration and pooled equally. Emulsion PCR, templating, and 550 chip loading were performed with an Ion Chef Instrument (Thermo Scientific MA, USA). Sequencing was performed on an Ion S5XL sequencer (Thermo Scientific MA, USA) as we did before.[38]

Data from the S5 XL run was processed using the Ion Torrent platform-specific pipeline software Torrent Suite v5.12 to generate sequence reads, trim adapter sequences, filter and remove poor signal reads and split the reads according to the barcode. FASTQ and BAM files were generated using the Torrent Suite plugin FileExporter v5.12. Automated data analysis was done with Torrent Suite Software using the Ion AmpliSeq RNA plugin v.5.12 and target region AmpliSeq_Mouse_Transcriptome_V1_Designed as we did before.[38]

Raw data was loaded into Transcriptome Analysis Console (4.0 Thermo Fisher Scientific, MA, EUA) and first filtered based on ANOVA eBayes using the Limma package and displayed as fold change. Significant changes had a p value <0.05 and FDR <0.2. Functional enrichment analyses were performed using Gene Set Enrichment Analysis (GSEA) with WEB-based Gene Set Analysis Toolkit (WebGestalt),[71] and STRING ranked enrichment (SRE).[72] The whole transcriptome gene list was ranked (linear fold change*-log10 FDR) and submitted to WebGestalt (http://www.webgestalt.org) or STRING (https://string-db.org/cgi/input?

sessionId=bFzQ6nknJDLN&input_page_show_search=on). Pathway enrichment was performed using the REACTOME database with default settings. Enrichment scores for gene sets were calculated using an FDR cutoff of 0.05.

Enriched pathways were manually recategorized to core transcriptomic modules and are displayed as a network (constructed using Cytoscape). Contingency analyses covering different microglial phenotypes were performed using Fisher's exact test and the Baptista-Pike method to calculate the odds ratio.

The RNA-seq data have been deposited to the Gene Expression Omnibus repository with the dataset identifier GSE244773.

Gene expression by qRT-PCR

RNA was extracted from flow cytometry sorted microglia using the Direct-zol RNA MiniPrep kit according to the manufacturer's instructions. cDNA synthesis was performed using 300 ng of total RNA (DNase I treated) with SuperScript III First-Strand Synthesis SuperMix. qRT-PCR was carried out using iQ SYBR Green Supermix on an iQ5 multicolor real-time PCR detection system (Bio-Rad). The expression of PCR transcripts was calculated using the $2^{-\text{deltaCt}}$ with *Yhwaz* serving as the internal control gene. Statistical analyses were performed on raw $2^{-\text{deltaCt}}$ values to detect differentially expressed transcripts between sampled groups.

The primers used in this study were purchased from Thermo Fisher Scientific; their sequences are provided in Table S11.

Phospho-proteomics sample preparations

Proteins (100–150 μg) from MACS-isolated microglia or synaptosomes (acutely prepared as before[37]) were processed for phosphoproteomic analysis following the solid-phase-enhanced sample-preparation (SP3) protocol. Enzymatic digestion was performed with trypsin/LysC (2 μg) overnight at 37°C at 1000 rpm. The resulting peptide concentration was measured by fluorescence. Enrichment for phosphorylated peptides was performed using Titanium dioxide beads (TiO2; ThermoFisher Scientific) as described in the manufacturer's protocol.

High-throughput proteomics data acquisition and quantification

Protein identification and quantitation were performed by nanoLC-MS/MS using an Ultimate 3000 liquid chromatography system coupled to a Q-Exactive Hybrid Quadrupole-Orbitrap mass spectrometer (Thermo Scientific, Bremen, Germany). Peptides of each sample were loaded onto a trapping cartridge (Acclaim PepMap C18 100 Å, 5 mm × 300 μm i.d., 160454, Thermo Scientific, Bremen, Germany) in a mobile phase of 2% ACN, 0.1% FA at 10 μL/min. After 3 min loading, the trap column was switched in-line to a 50 cm × 75 μm inner diameter EASY-Spray column (ES803, PepMap RSLC, C18, 2 μm, Thermo Scientific, Bremen, Germany) at 300 nL/min. Separation was achieved by mixing A: 0.1% FA and B: 80% ACN, 0.1% FA with the following gradient: 5 min (2.5% B to 10% B), 120 min (10% B to 30% B), 20 min (30% B to 50% B), 5 min (50% B to 99% B), and 10 min (hold 99% B). Subsequently, the column was equilibrated with 2.5% B for 17 min. Data acquisition was controlled by Xcalibur 4.0 and Tune 2.9 software (Thermo Scientific, Bremen, Germany).

The mass spectrometer was operated in the data-dependent (dd) positive acquisition mode alternating between a full scan (*m/z* 380–1580) and subsequent HCD MS/MS of the 10 most intense peaks from a full scan (normalized collision energy of 27%). The ESI spray voltage was 1.9 kV. The global settings were as follows: use lock masses best (*m/z* 445.12003), lock mass injection Full MS and chrom. peak width (FWHM) of 15 s. The full scan settings were as follows: 70 k resolution (*m/z* 200), AGC target 3×10^6, maximum injection time 120 ms; dd settings: minimum AGC target 8×10^3, intensity threshold 7.3×10^4, charge exclusion: unassigned, 1, 8, >8, peptide match preferred, exclude isotopes on, and dynamic exclusion 45 s. The MS2 settings were as follows: microscans 1, resolution 35 k (*m/z* 200), AGC target 2×10^5, maximum injection time 110 ms, isolation window 2.0 *m/z*, isolation offset 0.0 *m/z*, dynamic first mass, and spectrum data type profile.

The raw data were processed using the Proteome Discoverer 2.5.0.4 software (Thermo Scientific, Bremen, Germany). Protein identification analysis was performed with the data available in the UniProt protein sequence database for the *Mus Musculus* Proteome (2020_02 version, 55,398 entries) and a common contaminant database from MaxQuant (version 1.6.2.6, Max Planck Institute of Biochemistry, Munich, Germany). Sequest HT tandem mass spectrometry peptide database search program was used as the protein search algorithm. The search node considered an ion mass tolerance of 10 ppm for precursor ions and 0.02 Da for fragment ions. The maximum allowed missing cleavage sites was set as 2. For the phosphoproteomics, the IMP-ptmRS node, with the PhosphoRS mode (set to false), was used to localize phosphorylation sites. The Inferys rescoring node was considered, and the processing node Percolator was enabled with the following settings: maximum delta Cn 0.05; decoy database search target False Discovery Rate—FDR 1%; validation based on q-value. Protein-label-free quantitation was performed with the Minora feature detector node at the processing step. Precursor ion quantification used the processing step with the following parameters: Peptides: unique plus razor; precursor abundance was based on intensity; normalization mode was based on the total peptide amount; the pairwise protein ratio calculation and hypothesis test were based on a *t* test (background based). The Feature Mapper node from the Proteome Discoverer software was used to create features from unique peptide-specific peaks within a short retention time and mass range. This was achieved by applying a chromatographic retention time alignment with a maximum shift of 10 min and 10 ppm of mass tolerance, allowing for mapping features from different sample files. For feature linking and mapping, the minimum signal-to-noise (S/N) threshold was set at 5.

Further downstream analyses were performed using Proteome Discoverer 3.0. Peptide groups were filtered by modifications, excluding those that had no phosphorylation and contained oxidation or deamidation. Peptides with carbamidomethylation were

maintained. The table file with the final phosphoprotein list was extracted to Microsoft Excel and peptides were further filtered for each comparison using a custom-made Python script using the following parameters: (1) only master proteins detected with high/medium confidence FDR; (2) a protein/phosphoprotein must be detected in more than 50% of samples in each experimental group (except for proteins that were depleted entirely in one of the experimental groups); (3) the p-value adjusted using Benjamini–Hochberg correction for the FDR was set to <0.05; (4) at least 50% of samples with protein-related peptides sequenced by MS/MS; (5) the peptide spectrum matches (PSMs) was set to $\geq$3.

The mass spectrometry proteomic data have been deposited to the ProteomeXchange Consortium via the PRIDE partner repository with the dataset identifier PXD045719.

Phosphoproteome bioinformatic analyses

DE phosphoproteins of the datasets were inspected and cross-checked using the comprehensive web portal PhosphositePlus (https://www.phosphosite.org/homeAction.action [73]). Putative protein kinases controlling the phosphorylation of the filtered phosphopeptides were identified using NetworKIN 3.0 (http://networkin.info/index.shtml [74]). DE phosphoproteins were then screened for synaptic interactors/partners using Stitch and Mechismo.[75] Pathway enrichment analyses (FDR cutoff <0.05 with the Benjamini-Hochberg multiple test adjustments) were carried out in WebGestalt[71] and gProfiler with REACTOME and GO as functional databases. Only annotated proteins were included in the statistical background for pathway enrichment. Network construction and clustering were carried out using k-means clustering in STRING,[72] or Enrichment Map[76] and Omics Visualizer[77] in Cytoscape.

For phosphoproteomics analyses of microglia in the steady-state, $Rac1^{fl/fl}$ and $Cx3cr1^{CreER+}$ mice datasets were merged and filtered out using Python to assemble a unique phosphoprotein list compensating the modifications in the microglial phosphoproteome caused by Cx3cr1 haploinsufficiency.

For network integration of synaptic topographic maps, the set of DE phosphoproteins were first inputted in SynGO. The DE proteins/phosphoproteins were flagged to presynaptic or postsynaptic compartments using SynGO cellular components' anthology (dataset release version 20210225). DE proteins of datasets positively mapped to SynGO were subsequently screened for synaptic interactors/partners using protein-binding interfaces via inter-protein cross-links in the Stitch database (https://xlink.cncr.nl[78]).

Western blotting

Synaptosomes were denatured for 10 min at 95°C, separated in 10% SDS-PAGE, and transferred to nitrocellulose membranes. Membranes were blocked in 5% nonfat dry milk in TBS-Tween (TBS-T) for 1h and incubated overnight with primary antibodies at 4°C. Membranes were washed for 30 min with TBS-T buffer, incubated with peroxidase-conjugated secondary antibodies for at least 1h at room temperature and incubated for 5 min with SuperSignal West Pico PLUS Chemiluminescent Substrate. Images were acquired in a ChemiDoc System (Bio-Rad) and quantified using FIJI software.

Biosensor-based live-cell imaging

Imaging was performed using a Leica DMI6000B inverted microscope. The excitation light source was a mercury metal halide bulb integrated with an EL6000 light attenuator. High-speed, low-vibration external filter wheels (equipped with CFP/YFP/farRed excitation and emission filters) were mounted on the microscope (Fast Filter Wheels, Leica Microsystems). A 440-520nm dichroic mirror (CG1, Leica Microsystems) and a PlanApo 63×1.3NA glycerol immersion objective were used for CFP and FRET images. Images were acquired with 2 x 2 binning using a digital CMOS camera (ORCA-Flash4.0 V2, Hamamatsu Photonics). Quantifications were performed in FIJI,[67] as before,[68] using the precision FRET (PFRET) data processing software package for ImageJ (https://lvg.virginia.edu/digital-downloads/pfret-data-processing-software). The mean gray intensity values from ratio images were normalized using the deltaF/F0 for statistics. Representative images are shown in the intensity-modulated display.[68]

Protrusion Velocity Measurements in Cultured Microglia

Live cell imaging was conducted to assess the protrusion velocity of HCM3 microglia. A Leica FFW inverted microscope equipped with a temperature-controlled chamber and a CO_2 incubator was utilized to maintain optimal cell conditions. The cells were co-transfected with plasmids encoding Rac1-DN or wild-type Rac1 (WT Rac1) and mCherry-lifeact to visualize actin dynamics. To facilitate cell adhesion, plastic bottom dishes coated with poly-D-lysine were used. Imaging was performed at 10-min intervals over a total duration of 5 h. During imaging, appropriate filter sets were employed to visualize the mCherry fluorescence emitted by the cells. Time series were acquired using a 40x objective, ensuring comprehensive coverage of the entire cells and enabling clear visualization of microglial protrusions. Low-intensity illumination and short exposure times were employed to minimize photobleaching and phototoxicity, thereby preserving the integrity of the cells during the imaging process.

Kymographs were generated from the acquired time-lapse images using Fiji/ImageJ software to quantify the protrusion velocity. The mCherry-lifeact channel was used to identify the leading edge of microglial protrusions. Manual tracking was performed by tracing the outline of individual protrusions over time to extract positional information. The "Segmented Line" tool in ImageJ was utilized to measure the distance traveled by the leading edge between consecutive time points. The time intervals between frames were used to calculate the velocity of protrusion extension. The protrusion velocity assessments were performed by an experimenter blinded to the experimental conditions.

Collection of microglia-conditioned media (MCM)

Cultures were infected with lentiviruses carrying pLKO-empty, pLKO-Rac1 shRNA, or Cre recombinase as before.[7,37,69] Replication-incompetent lentiviral particles were prepared as before.[7,69,66] After viral removal and medium refeed, microglia were cultured for 5–7 days. Then, the culture medium (MCM) was collected, centrifuged for debris removal (1200 rpm, 5 min), and frozen at −80°C until used.

We chose to use neonatal microglial cells and embryonic rat neuronal cultures in our live-cell imaging experiments with neurons (see below). By using neonatal microglial cells from rats, we were able to synchronize the developmental stage of the microglia and neurons within a single species, which was crucial for accurately replicating *in vivo* conditions in our *in vitro* experiments. Using viral-mediated knockdown, we manipulated Rac1 expression levels in primary neonatal rat microglial cultures and investigated its impact on the neurons while ensuring compatibility with the developmental stage and species of the neuronal cultures.

Single-spine calcium imaging

Cortical neurons were plated on plastic-bottom culture dishes (μ-Dish 35 mm, iBidi) and co-transfected using the calcium phosphate method, as before,[7,37,69] with mCherry-Lifeact-7 and pGP-CMV-GCaMP6f. Experiments were carried out by recording neuronal cultures with microglia-conditioned media (MCM) for 10 min (baseline) and then in the presence of MCM + KCl 20 mM (neuronal stimulation) for additional 10 min.

Imaging was performed using a Leica DMI6000B inverted microscope. The excitation light source was a mercury metal halide bulb integrated with an EL6000 light attenuator. The L5 (Ex: 460–500; BS: 505; Em: 512–542) and TX2 (Ex: 540–580; BS: 595; Em: 607–683) filter set and a PlanApo 63×1.3NA glycerol immersion objective were used. Images were acquired with 2 x 2 binning using a digital CMOS camera (ORCA-Flash4.0 V2, Hamamatsu Photonics). The mean gray intensity values from spine GCaMP6f were normalized using the deltaF/F.

Data for activity-dependent spine calcium dynamics were fit using a beta growth and decline model (Y=Ym*(1+ (Te - X)/(Te - Tm))*(X/Te)^(Te/(Te-Tm))) during spine expansion or a plateau followed by one-phase exponential decay (Y= IF(X < X0, Y0, Plateau+(Y0-Plateau)*exp(-K*(X-X0)))) during spine retraction. Spines that collapsed or were eliminated during the evoked neuronal activity were excluded from the analysis. The additional parameters were used for data exclusion: spine expansion <2.5% spine area; spine retraction <2% spine area; calcium signal <25% amplitude increase.

QUANTIFICATION AND STATISTICAL ANALYSIS

Experimenters were blinded to genotypes and housing conditions. Data were tested for Gaussian distribution using the D'Agostino-Pearson omnibus test. All tests considered mice or specific cells as experimental units with a significance level of $p < 0.05$. For behavioral tests and Sholl/colocalization, randomized-block two-way ANOVA with Turkey correction was used. Flow cytometry for three genotypes employed ANOVA with Benjamini, Krieger, and Yekutieli correction. The effects of EE or CE between genotypes were analyzed using two-way ANOVA with Šidák correction. Gene expression was assessed by qRT-PCR using the Mann-Whitney test. Biosensor live-cell imaging utilized repeated measures of two-way ANOVA with Greenhouse-Geisser and Šidák corrections. Protrusion velocity in microglia was analyzed using two-way ANOVA with the Šidák correction. Lastly, single-spine calcium imaging was conducted with single spines as experimental units using the Mann-Whitney test.

Descriptive statistics for each dataset are defined in Figure Legends. Statistical analysis and graph construction were performed in GraphPad Prism version 9.0.2 for macOS. Figure panels were assembled in Adobe Illustrator 2020 (version 24.3). Illustrations were assembled in BioRender.